1    **Integration of microseism, wavemeter buoy, HF Radar and hindcast data to analyze the**

2    **Mediterranean cyclone Helios**

4    **Alfio Marco Borzì[1*], Vittorio Minio[1], Raphael De Plaen[2], Thomas Lecocq[2], Salvatore**

5    **Alparone[3], Salvatore Aronica[4], Flavio Cannavò[3], Fulvio Capodici[5],  Giuseppe Ciraolo[5],**

6    **Sebastiano D'Amico[6], Danilo Contrafatto[3], Giuseppe Di Grazia[3], Ignazio Fontana[4],**

7    **Giovanni Giacalone[4], Graziano Larocca[3], Carlo Lo Re[7], Giorgio Manno[5], Gabriele**

8    **Nardone[7], Arianna Orasi[7], Marco Picone[7], Giovanni Scicchitano[8], Andrea Cannata[1,3]**

9    [1]Dipartimento di Scienze Biologiche, Geologiche ed Ambientali - Sezione di Scienze della Terra, Università degli
10   Studi di Catania, Catania, Italy;

11   [2]Seismology-Gravimetry, Royal Observatory of Belgium, Brussel, Belgium;

12   [3]Istituto Nazionale di Geofisica e Vulcanologia - Sezione di Catania, Osservatorio Etneo, Catania, Italy;

13   [4]Institute of Anthropic Impacts and Sustainability in the Marine Environment - National Research Council (IAS-
14   CNR), Campobello di Mazara, TP, Italy

15   [5]Dipartimento di Ingegneria Civile, Ambientale, Aerospaziale, dei Materiali, University of Palermo, 90128
16   Palermo, Italy

17   [6]Department of Geosciences, University of Malta, Msida, Malta;

18   [7]Centro Nazionale per la Caratterizzazione Ambientale e la Protezione Della Fascia Costiera, la Climatologia
19   Marina e l'Oceanografia Operativa, Italian National Institute for Environmental Protection and Research, Rome,
20   Italy.

21   [8]Dipartimento di Scienze della Terra e Geoambientali, Università degli Studi di Bari Aldo Moro, 70125 Bari, Italy

22   *Corresponding author

23   alfio.borzi@phd.unict.it

24   Corso Italia 57, 95129 Catania (Italy)

26  **Keywords:** Microseism, wavemeter buoy, HF Radar, Mediterranean cyclones, climate change,

27  monitoring sea state

28  **Abstract**

29  In this work, we study a Mediterranean cyclone, called Helios, took place during the period 9-

30  11 February 2023 in the southeastern part of Sicily and Malta Island, by a multiparametric

31  approach combining microseism results with sea state and meteorological data provided by

32  wavemeter buoy, HF Radar, hindcast maps and satellite SEVIRI images. The sub-tropical

33  system Helios caused heavy rainfall, strong wind gusts and violent storm surges with

34  significant wave heights greater than 5 meters. We deal with the relationships between such a

35  system and the features of microseism (the most continuous and ubiquitous seismic signal on

36  the Earth) in terms of spectral content, space-time variation of the amplitude and source

37  locations tracked by means of two different methods (amplitude-based grid search and array

38  techniques). By comparing the location of the microseism sources and the area affected by

39  significant storm surges, derived from sea state data, we note that the microseism location

40  results are in agreement with the real position of the storm surges. In addition, we are able to

41  obtain the seismic signature of Helios using a method that exploits the coherence of continuous

42  seismic noise. Hence, we show how an innovative monitoring system of the Mediterranean

43  cyclones can be designed by integrating microseism information with other techniques

44  routinely used to study meteorological phenomena.

46  **1. Introduction**

47  Significant storm surges driven by intense low-pressure systems represent one of the main

48  hazards to the Mediterranean coastal areas causing flooding, beach erosion and damage to

49  infrastructures and cultural heritages (Flaounas et al., 2022; Lionello et al., 2019;).

50  Occasionally, when there are favorable conditions like high sea temperature and high contrast

of temperature sea-air, the cyclones can acquire the characteristics of a MEDIterranean hurriCANE (hereinafter Medicane). Medicanes genesis is favored when an extratropical depression gets isolated from the polar jet stream. The "cut-off" feature, when situated above the Mediterranean Sea, remains relatively stable and takes advantage of the abundant heat and humidity from the sea to generate organized convection (Faranda et al., 2022).

The structure of a Medicane is characterized by the presence of a central free-cloud "eye", a strong rotation around the pressure minimum, an eyewall with convective cells, from which rain bands extend. It, that can be considered like a small-scale tropical cyclone, can lead to sea-level rise, storm surge and sea waves that can reach significant heights of about five meters (Miglietta and Rotunno, 2019). The typical Medicane lifetime is limited to a few days, generally from 2 to 5 days, as a result of the small areal extension of the Mediterranean Sea that represents their main energy source; for the same reason also the diameter is generally restricted to a range between 100 and 300 km (Comellas et al., 2021), and their intensity rarely exceeds the category 1 of the Saffir-Simpson hurricane wind scale (Miglietta end Rotunno., 2019). In addition, due to the geometrical and meteorological characteristics of the Mediterranean Sea, a Medicane reaches fully tropical characteristics (a symmetric, deep warm-core structure and convection in their development and maintenance) for a short time, while extratropical features (non-symmetrical structure and not well-developed convection around the core) prevail for most of their lifetime (Miglietta et al., 2011, 2013). As yet, there is no clear separation between tropical and extratropical cyclones, and the first approach to differentiate these cyclones was developed by Hart (2003). This method, called cyclone phase space analysis, relies on a large spectrum of different cyclone types by using several parameters such as the symmetry/asymmetry and the cold or warm core. In this way, as explained by the author, an objective classification of cyclone phase is possible, merging the basic structural description of tropical, extratropical, and hybrid cyclones into a continuum. The favorable

76    months to the Medicanes generations are the autumn and early winter months (from September

77    to January). Indeed during these months, the Mediterranean Sea preserves high temperatures

78    after the summer season, and the first cold upper-air troughs are observed, thus creating a high

79    sea-air temperature gradient (Cavicchia et al., 2014; Nastos et al., 2018). Specifically, the

80    occurrence of intense convective instability is initiated when the polar jet stream transports

81    cold air masses over the warmer Mediterranean Sea (Cavicchia et al., 2014; Nastos et al., 2018).

82    The Medicanes generation during the late-winter months (February and March) is possible but

83    less common (Cavicchia et al., 2014, Tous and Romero, 2013).

84    These Mediterranean extreme weather events caused damages, floods, deaths, and injuries in

85    several Mediterranean coastal areas (South France, Central and South Italy, Malta, Balearic

86    islands, Greece, Crete, Turkey, and some African states; Androulidakis et al, 2022; Bouin and

87    Brossier, 2020; Carrió et al., 2017; Dafis et al., 2018; Di Muzio et al., 2019; Faranda et al.,

88    2022; Kerkmann and Bachmeier, 2011; Lagouvardos et al., 2022; Pravia-Sarabia et al., 2021;

89    Portmann et al., 2020; Rumora et al., 2018; Varlas et al., 2020; Zimbo et al., 2022). As

90    explained by Cavicchia et al. (2014), the most frequent genesis regions are the Balearic Islands

91    and the Ionian Sea. In particular, during the last 12 years, the majority of the Medicanes have

92    been developed over the Ionian Sea and this is probably linked to the sea surface temperature

93    that, as shown by Shaltout and Omstedt (2014), in the Ionian Sea is constantly 1.0°-1.5° C

94    higher than that in the Tyrrhenian Sea.

95    Although these extreme Mediterranean events showed significant wave heights (hereinafter

96    SWH, defined as the average wave height of the highest one-third of the waves), comparable

97    to the common seasonal storms, they caused greater coastal flooding (Scardino et al., 2022;

98    Scicchitano et al., 2021). The strong winds, generated during a Medicane, cause the

99    development of powerful wave motions and lead to an energy transfer from the sea waves to

100   the solid Earth (Borzì et al., 2022). This energy transfer between the atmosphere, the

101      hydrosphere and the solid Earth is one of the generation mechanisms of the most continuous

102      and ubiquitous seismic signal on the Earth, called microseism (e.g. Hasselmann, 1963;

103      Longuet-Higgins, 1950). In connection with the spectral content and the source mechanism

104      (e.g. Haubrich and McCamy, 1969), it is possible to divide this signal into: primary microseism

105      (PM), that shows the same period as the oceanic waves (13 - 20 s) and low amplitudes, and is

106      generated by the energy transfer of oceanic waves breaking against the shoreline (Ardhuin et

107      al., 2015; Hasselmann, 1963); secondary microseism (SM), generated by sea waves with the

108      same frequency traveling in opposite directions and exhibiting frequency about twice of the

109      frequency of the oceanic waves (period of 5 - 10 s) and amplitude higher than the PM (e.g.

110      Ardhuin and Roland, 2012; Ardhuin et al., 2015; Lepore and Grad, 2018; Longuet-Higgins,

111      1950; Oliver and Page, 1963); short-period secondary microseism (SPSM), that has a period

112      shorter than 5 seconds and is generated by the interaction between local wave motions near the

113      coastline (Bromirski et al., 2005).

114      Several works deal with the relationship between microseism and the sea state (Ardhuin et al.,

115      2019; Cannata et al., 2020; Guerin et al., 2022; Moschella et al., 2020), while others take into

116      account specifically the relationship between microseism and cyclonic activity (e.g.,

117      Bromirski, 2001; Bromirski et al., 2005; Gerstoft et al., 2006; Gualtieri et al., 2018; Lin et al.,

118      2017; Retailleau and Gualtieri, 2019, 2021; Zhang et al., 2010) considering in particular

119      typhoons (Lin et al., 2017), tropical cyclones (Zhang et al., 2010), and hurricanes (Gerstoft et

120      al., 2006). Interestingly, Bromirski (2001) and Bromirski et al. (2005) showed that the

121      microseism bands most affected by the presence of a cyclone are the SM and SPSM ones.

122      For the first time, the relationship between SM, SPSM, and Medicane was analyzed by Borzì

123      et al. (2022), who considered the Medicane Apollo to reconstruct both the seismic variation in

124      terms of power spectral density (PSD), root mean square (RMS) amplitude and the Medicane

125      position during its lifetime by two different methods (array analysis and grid search method by

126  means of seismic amplitude decay). In this work, we explore the relationship between

127  microseism and the Sub-Tropical system "Helios" that occurred in the Sicily Channel during

128  the period 9-11 February 2023 (**Figure 1**). The microseism results are integrated with

129  wavemeter buoy, HF Radar, hindcast and satellite data (SEVIRI Images) to perform an

130  investigation as comprehensive as possible of this extreme Mediterranean meteo-marine event.

131  **2. Sub-tropical system "Helios" (9-11 February 2023)**

132  During the period 9-11 February 2023, a low-pressure system, later renamed Helios, developed

133  over the Sicily Channel due to the strong contrast between the very cold air, coming from NE

134  (Balkans area) and the relatively warm sea surface. From satellite data, the warm core anomaly

135  of this cyclone is evident, requisite for the development of the Medicane. However, this storm

136  failed to become a Medicane, for which it is necessary that the cyclone maintains well-

137  developed convection around the eye, absent in this case probably due to a little interaction

138  between sea-air caused by sea surface temperature not suitable for the development of a

139  Medicane                (https://twitter.com/medcyclones/status/1623795373423620096?s=20;

140  https://twitter.com/medcyclones/status/1623992335104081921?s=20;

141  https://twitter.com/medcyclones/status/1624143740800536591?s=20; last access 23/05/2023;

142  D'Adderio et al., 2023).

143  In spite of this, Helios, thanks to its proximity to the Sicilian and Maltese coasts, was able to

144  produce damage along these areas. The effects of the sub-tropical system Helios were

145  significant, especially in Catania, Ragusa and Siracusa provinces (located in the south-eastern

146  part of Sicily), the Sicilian Meteorological service ("Regione Siciliana—SIAS—Servizio

147  Informativo Agrometeorologico Siciliano", http://www.sias.regione.sicilia.it/) recorded heavy

148  rainfall, more than 200 mm/48 h and peaks of about 500 mm/48 h near Noto for the days 9-10

149  February 2023, heavy snowfall starting from 1200 m a.s.l. with accumulations of fresh snow

150  on Etna thicker than two meters, strong wind gusts up to 90 km/h along the exposed coast

151 (Davies, 2023) and severe storm surge with SWH greater than 5 meters. Similar effects were

152 also recorded in Malta. The minimum pressure value in the cyclone eye amounted to 1002 hPa.

153 An overview of the positions and the extension of the sub-tropical system Helios is represented

154 in **Figure 1.**

155 As a consequence of the damage caused by Helios, the Regional Sicilian Government decided

156 to require a national state of emergency for 12 months for all the municipalities of Catania,

157 Siracusa, and Ragusa provinces and some municipalities of Messina province

158 (https://www2.regione.sicilia.it/deliberegiunta/file/giunta/allegati/N.099_15.02.2023.pdf, last

159 access 23/05/2023).

160

161 **3. Data and Methods**

162 We analyzed the data recorded in the period 8 to 13 February 2023 comprising the development

163 of Helios, the climax in terms of minimum pressure value, wind velocity, precipitation intensity

164 and SWH, and its decline.

165 **3.1. Seismic data**

166 We used 105 seismic stations installed along the Italian and French coastal areas, in the Sicily

167 channel coastlines (in Malta, Lampedusa and Linosa islands), in Corsica island and along the

168 Greek coastal areas to perform spectral analysis, localization analysis by the grid search method

169 based on seismic amplitude decay and to obtain the seismic signature of the analyzed event

170 (**Figure 2a** and **Supplementary Table 1**). Three of these stations (IWAV2, IWAV3 and

171 IWAV5) were installed as part of the i-waveNET "Implementation of an innovative system for

172 monitoring the state of the sea in climate change scenarios" project, funded by the Interreg

173 Italia-Malta Programme (https://iwavenet.eu/; notice 2/2019 Axis 3; project code C2-3.2-106).

174 The aim of this project is to set up an innovative sea state monitoring network, integrating

175 different measurement technologies, such as HF radars, seismic stations, sea level probes, wave

176    buoys and weather stations. Additionally, 15 seismic stations, installed in the Etnean area, were

177    used to conduct array analysis (**Figure 2b** and **Supplementary Table 2**). The selected seismic

178    stations show specific characteristics: they are i) installed near the coastal areas and ii) equipped

179    with 3-component broadband seismic sensors.

**3.2. Sea state measures**

181    In this work, we use sea state data derived from four independent methodologies. In particular,

182    we used: i) significant wave height (SWH-Hind), provided by the hindcast maps produced by

183    Copernicus; ii) significant wave height (SWH-Buoy), period and direction of the waves

184    measured by the wavemeter buoy installed near Mazara del Vallo; iii) significant wave height

185    (SWH-HF), period and direction of the waves obtained by the HF Radar installed at the Marina

186    di Ragusa harbor; iv) SEVIRI Images to spatially and temporally track the position of the

187    cyclone. These four different data sources have been used to both describe the sea state

188    evolution during the Helios event, and characterize the physical state of the sea which is strictly

189    correlated to the microseism derived outputs.

**3.2.1. Copernicus Data**

191    Regarding the description of the Helios event in terms of spatio/temporal distribution of SWH,

192    wave period and direction over the whole domain, we referred to the

193    "MEDSEA_HINDCAST_WAV_006_012" product, provided by the Copernicus Marine

194    Environment Monitoring Service (CMEMS) (Korres et al., 2019). The CMEMS product

195    contains the hindcast maps of the Mediterranean Sea Waves forecasting system and is based

196    on the third-generation wave model WAM Cycle 4.5.4  composed by hourly wave parameters

197    at 1/24° horizontal resolution (Korres et al., 2019).

### 3.2.2 Wavemeter buoy data

Concerning the wave buoy, in **Figure 2c** we show the locations of this buoy, located offshore of Mazara del Vallo, at a depth of 85 m. The Mazara buoy is managed by ISPRA and is part of the National Wave Buoy Network (RON). The instrumental equipment consists of buoys allowing the acquisition of wave parameters in real time. The long time series represent an important heritage for the knowledge of marine phenomena affecting the Italian seas, both in terms of climatology and extreme events. The RON National Wave Network is now composed of 7 stations located off the Italian coasts for the continuous measurement of wave and meteorological parameters, such as wind direction and speed, atmospheric pressure, water surface and air temperatures, with real-time data transmission. Until 2014, the ISPRA wave buoy network was equipped with WatchKeeper™ weather wave meters manufactured by the Canadian company AXYS Ltd. (Bencivenga et al., 2012). The new meteo-marine buoys were developed, designed and built in Italy for the specific needs of ISPRA. Data are collected continuously for periods of 20-25 minutes and are provided every 30 minutes.

The parameters recorded by the wavemeter buoy and used in this study are: i) SWH (m), ii) wave mean period (s) and iii) wave mean direction (°).

### 3.2.3. HF Radar data

Sea state measures are also provided by the HF system located in the Marina di Ragusa harbor (**Figure 2c**) which is owned by the CNR-IAS (Consiglio Nazionale delle Ricerche - Istituto per lo Studio degli Impatti Antropici e Sostenibilità in Ambiente Marino). This HF radar is part of the CALYPSO HF network operating in the Malta-Sicily channel since 2013. The network is nowadays composed of seven HF Codar SeaSonde systems transmitting at 13.5 MHz (central frequency). The network provides sea surface current maps at 3 km of spatial resolution at hourly scale (Capodici et al., 2019). Each HF radar provides sea state variables (SWH-HF,

222  wave period, wave direction) every 15 minutes; these data are referred to 10 independent

223  annular rings 3 km wide, centered at the HF site location. Data used in this work regard the last

224  annular ring (30 km far from the HF site) showing the best temporal continuity of the

225  measurements. The sea state derived by the HF technology has been deeply validated by several

226  authors (e.g. Long et al., 2011; Lorente et al., 2021; Orasi et al., 2019; Saviano et al., 2019).

227  **3.2.4. Satellite data**

228  The passage of the Helios cyclone in the study area was tracked by means of the High Rate

229  SEVIRI Level 1.5 Image Data. The Level 1.5 image data represents the geolocated and

230  radiometrically pre-processed images that are prepared for subsequent processing steps, e.g.

231  the extraction of meteorological products helpful in our case study. For further information

232  about    this    methodology    you    can    see    the    EUMETSAT    website

233  (https://navigator.eumetsat.int/product/EO:EUM:DAT:MSG:HRSEVIRI    last    access

234  25/05/2023). In particular, an image at 10.8 μm each 15' was downloaded and analyzed.

235  **3.3. Spectral Analysis of Microseism**

236  The seismic data were corrected for the instrument response and thereafter spectral and

237  amplitude analyses were performed. For the spectral analysis, hourly spectra of the seismic

238  signal were calculated by applying Welch's method (Welch, 1967) with time windows of 81.92

239  s. The hourly spectra, thus obtained, were gathered and represented as spectrograms, with time

240  on the x-axis, frequency on the y-axis, and the $\log_{10}$ of the PSD indicated by a color scale.

241  Some spectrograms obtained from the vertical component of 4 stations are shown in **Figure 3**.

242  Concerning the amplitude, we estimated hourly RMS amplitude time series for the typical

243  microseism frequency bands: 0.2-0.4 Hz (SPSM, **Supplementary Figure 1**), 0.1-0.2 Hz (SM,

244  black lines in **Figure 3**) and 0.05-0.07 Hz (PM, **Supplementary Figure 2**).

245 In addition, to show the spatial and temporal distribution of the RMS amplitude during the

246 period under investigation, we plotted the mean RMS amplitude computed on non-overlapped

247 1-day-long moving windows for the three microseism bands (**Figure 4, Supplementary**

248 **Figures 3 and 4**). Each dot, in **Figure 4** and in **Supplementary Figures 3 and 4,** represents a

249 seismic station and the color of the dot relates to the corresponding RMS amplitude at that

250 location, as specified in the color bar. Noteworthy, the colorbar of the PM band

251 **(Supplementary Figure 3)** shows a different range of RMS amplitude highlighting a different

252 response between the PM and the SM and SPSM bands to the sub-tropical system Helios

253 (**Figure 4** and **Supplementary Figure 4**). Furthermore, in these figures, we compared the RMS

254 amplitude with the SWH, represented by the contour lines. A detailed description of all the

255 figures cited in this paragraph is given in section 4.2.

256 **3.4 Correlation analysis between microseism amplitude and significant wave height**

257 The calculation of correlation coefficients between the RMS amplitude time series and the

258 significant wave height time series was conducted in accordance with previous studies (e.g.,

259 Bromirski, 2001). This calculation was performed for each grid cell of the hindcast maps during

260 the investigated period to obtain information about the spatial variabilityof the correlation

261 coefficients. This kind of analysis provides information about the location of the main sources

262 of the microseism recorded by the 4 selected stations. To explore the non-linear relationship

263 between seismic RMS amplitudes and significant wave heights, we followed the approach

264 proposed by Craig et al. (2016) and employed the Spearman correlation coefficient. The

265 Spearman correlation coefficient is defined as a nonparametric measure of rank correlation

266 (Craig et al., 2016). Correlation maps, gathering together the correlation values obtained in the

267 nodes of the whole Mediterranean Sea, were obtained for the vertical component of each station

268 and the 3 typical microseism frequency bands (Figure 5).

**3. 5. Tracking Helios position by Microseism**

Following Borzì et al. (2022), we used two different and complementary methods to track the position of the sub-tropical system Helios from a seismic point of view. In particular, we use i) a grid search method based on the seismic amplitude decay and ii) array analysis. These methods allow us to track the evolution over time of the location of the centroid of the seismic sources generated by the sea state variations induced by the cyclone. Such seismic data were compared with the cyclone trajectory which was identified by processing the High Rate MSG SEVIRI images. This latter task was accomplished by visually identifying the positions of the cyclone's eye which was clearly identifiable only between 01:00 and 23:00 of the 10 February 2023.

**3.5.1. Grid search method**

We used the seismic signals recorded by 105 seismic stations (**Figure 2a**) to map out the position of Helios during the analyzed period by employing a grid search approach (**Figure 6**). The region, where we executed the grid search, is a bi-dimensional area of 1760 km x 2400 km (minimum longitude: 5°; maximum longitude: 30°; minimum latitude: 30°; maximum latitude: 46°) with a spacing of 1°. As shown by several authors who used seismic amplitude decay methods, both to locate microseism sources (Borzì et al. 2022) and seismo-volcanic sources (Battaglia and Aki, 2003; Cannata et al., 2013; Kumagai et al., 2011), the grid spacing is chosen as a compromise between good spatial resolution and reasonable computation time. The microseism source is localized based on the goodness of the linear regression fit (hereafter referred to as $R^2$) computed for each node of the bi-dimensional (2D) grid previously mentioned. Specifically, the source was identified at the centroid position of all the grid nodes where the R2 values deviate by no more than 1% from the maximum R2 value. In this method, we used an RMS signal window of 4 hours and thus we were able to obtain 1 localization every

293   4 hours. In addition, following Borzì et al. (2022), we applied a method to evaluate the

294   statistical significance of the retrieved maximum $R^2$ value and to test the confidence of the

295   location results. Specifically, we conducted 20 iterations by randomly rearranging the RMS

296   amplitude values among the stations. Then, we calculated the 95th percentile and we obtained

297   a value of 0.27. In accordance with this result, we consider reliable the localizations with $R^2$

298   values greater than 0.27. To retrieve the errors associated with each localization, the bootstrap

299   technique is used (Johnson, 2001). This technique consists in recalculating each source location

300   1000 times, by randomly resampling the data (amplitude-distance pairs) with repetition.

301   It must be underlined that the grid search method used in this study shows various limits that

302   in specific cases can invalidate the source locations. In particular, the first limit concerns the

303   fact that in this method we consider the microseism source as a point-like source, while the

304   microseism is produced in a wide area of the Mediterranean Sea. In this scenario, the

305   localization of the point-like source is determined as the barycentric point of the extended

306   source. However, it is important to consider a limitation of this method related to the presence

307   of multiple sources with similar amplitude in the same frequency range. In such cases, the

308   constrained source location shifts towards a position between the actual seismic source

309   locations (Battaglia et al., 2005), resulting in a significant decrease in $R^2$. In our case, we

310   neglect localization showing $R^2$ values smaller than 0.27, to avoid unreliable localization.

311   **3.5.2. Array analysis**

312   In order to track the location of the sub-tropical system Helios using array techniques, we

313   considered fifteen stations belonging to the Mt. Etna seismic permanent network and used them

314   as a roughly circular array (**Figure 2b**).

315   The Array Response function (ARF) is a good tool to plan the array geometry required to

316   investigate microseism signals or, in this case, to evaluate the performance of a pre-existing

317 array in microseism studies. The ARF, previously obtained by Borzì et al. (2022), exhibits that

318 the roughly circular array has a good response for the PM and SM cases.

319 In this study, we employed the f-k (frequency-wavenumber) analysis technique on microseism

320 signals (e.g. Rost and Thomas, 2002). This approach involves a spectral domain beamforming

321 method that utilizes a grid search of slowness to determine the back azimuth and apparent

322 velocity values that maximize the amplitude of the combined array traces. The result of the f-

323 k analysis is the PSD as a function of slowness. In accordance with Borzì et al. (2022), we

324 followed the subsequent processing steps to implement array analysis on microseism data: (i)

325 demeaning and detrending; (ii) applying a specific frequency band filter for microseism; (iii)

326 segmenting the data into tapered windows of 120 seconds each; (iv) excluding windows

327 containing seismo-volcanic amplitude transients (such as volcano-tectonic earthquakes, long-

328 period events, and very long-period events) identified using the STA/LTA technique (e.g.,

329 Trnkoczy, 2012); (v) performing f-k analysis for each window by conducting a slowness grid

330 search (ranging from -1 to 1 s/km in the east and north components of the slowness vector)

331 with a spacing of 0.05 s/km. An illustrative example of the outcomes is presented in Figure 6.

332 For further details about these two methods used in this work, you can see Borzì et al. (2022).

333 **3.6. Seismic signature of the Medicanes**

334 In a way to obtain the seismic signature and the main spectral characteristics of the sub-tropical

335 system Helios, we use a method developed by Soubestre et al. (2018). This method was initially

336 developed as a network-based method to detect and classify seismo-volcanic tremors. The

337 proposed method utilizes the coherence of tremor signals within the network, which is

338 determined based on the array covariance matrix. Using this technique, as explained by

339 Soubestre et al. (2018), it is possible to highlight both volcanic tremors and other types of

340 seismic sources such as tectonic earthquakes (local, regional, and teleseismic), and oceanic

seismic noise (microseism). This method allows the identification of the spatially coherent individual noise source within a specific network, identified as small spectral width, as opposed to other noises such as local effects that would generate multiple individual sources. For further details about the method, see Soubestre et al. (2018).

In this study, we are interested in detecting the microseism produced by the sub-tropical system Helios. Since we are interested in such a microseism, we filtered the signal in the band 0.1-1 Hz and resample it to 25 Hz in a way to reduce the computation time. To compute the covariance matrix we use only the vertical component of the seismic signal and a window length of 60 seconds. The analyses were performed using the data recorded by a station set comprising both stations installed near the south Sicilian coast (CLTA and IWAV5) and in the Malta (MSDA) and Linosa (LINA) islands in order to have the microseism source within the selected station set.

## 4. Results and Discussion

We analyze the sea state, derived by four independent techniques, and the seismic data recorded by the i) 105 seismic stations represented in **Figure 2a** and by ii) the 15 Etnean seismic stations (**Figure 2b**) during the period 8-13 February 2023. We chose a period longer than the real lifetime of the sub-tropical system Helios in a way to include the development, the climax in terms of meteorological events that occurred during the days 9-10 February, and the following loss of intensity.

### 4.1. Sea state

In **Figure 7**, we show the SWH, the mean wave period and the direction time series recorded during the period 8-13 February 2023 by the buoy of Mazara del Vallo (**Figure 7b, d and f**) and the HF radar installed in Marina di Ragusa harbor (**Figure 7a, c and e**).

365    The buoy data indicates that the sea storm reached its maximum significant wave height of 3.1

366    m at 20:00 on 9 February, with a mean direction of 140° indicating that waves were generated

367    by Scirocco wind, which is the main wave direction for the period under investigation and a

368    period that varies from 5 to 9 s. The data from HF Radar, installed closer to the cyclone position

369    than the buoy, show a maximum SWH of about 6 m recorded on 9 February at 22:30, the mean

370    wave direction was of 100° approximately and the period varies in the range of 5-12 s. Both

371    datasets allowed defining the time interval of the wave storm which spanned between 8-13

372    February 2023. The higher SWH measured by the HF radar agrees with the shorter distance

373    from the cyclone eye (~90 km) of this instrument compared to that of the wave buoy (~190

374    km).

375    The spatio-temporal distribution of the SWH in the whole area is shown by the hindcast maps

376    in **Figure 8**. Noticeably that the stronger effect of the sub-tropical system Helios on the sea

377    state of the Malta-Sicily channel was the increase of the SWH during 9 - 10 February. On 9

378    February the higher SWH values were recorded mainly in the patch of the sea at the east of

379    Sicily Island and of the Maltese archipelago, whereas the wave storm invaded the whole Malta-

380    Sicily channel on 10 February. Finally, on 11 February the wave storm started moving to the

381    south, reaching the northern part of the African coasts.

382    The comparison between SWH-Hind and SWH-HF revealed a good agreement ($R^2$~0.85) even

383    if an underestimation of the event by the CMS model (slope of ~0.7) was observed

384    (**Supplementary figure 6**).

385    **4.2. Spectral Analysis and RMS spatial distribution**

386    To perform the spectral analysis, we used the 105 seismic stations installed along the Italian,

387    Greek and Maltese coastal areas. In **Figure 3,** we plot the spectrograms and the RMS amplitude

388    time series (black lines), obtained by analyzing the vertical component of the seismic signals

389    recorded by four stations installed in Malta (MSDA **Figure 3a**), on Linosa Island (LINA

390   **Figure 3b**), near Pozzallo (IWAV5 **Figure 3c**) and in Central Italy (CELB **Figure 3d**). We

391   chose these four stations to compare the results obtained from the stations installed near the

392   sub-tropical system (LINA, MSDA and IWAV5), with the result obtained from the far station

393   (CELB).

394   As shown by Borzì et al. (2022), in the spectrograms a great part of the energy is focused in

395   the 0.1-1 Hz band, corresponding with the SM and SPSM bands. In addition, it is also evident

396   how the considered stations show a different behavior, in terms of both spectrograms (**Figure**

397   **3**) and RMS amplitude time series (**Figure 3** and **Supplementary Figures 1** and **2**), that

398   depended on their position. In particular, spectrograms and RMS amplitude time series

399   obtained from the data recorded by MSDA (**Figure 3a** and **Supplementary Figure 1a** and **2a**),

400   LINA (**Figure 3b** and **Supplementary Figures 1b** and **2b**) and IWAV5 (**Figure 3c** and

401   **Supplementary Figures 1c** and **2c**) stations, installed close to Helios (**Figure 1** and **Figure**

402   **2**), show the maximum PSD and RMS amplitude values during the time interval 9-11 February

403   2023, highlighted by the vertical dashed lines in **Figure 3**. On the other hand, the spectrogram

404   and RMS amplitude time series of the station CELB (**Figure 3d** and **Supplementary Figures**

405   **1d** and **2d**), installed in the Tyrrhenian area, exhibited the maximum PSD and RMS amplitude

406   values a few days before Helios at the same time as a local storm surge.

407   To show the space-time distribution of the RMS amplitude, we calculate the daily RMS average

408   for the three main microseism bands (PM and SPSM in **Supplementary Figures 3** and **4**, SM

409   in **Figure 4**) during the period 8-13 February 2023. All the three analyzed microseism bands

410   show a relationship with the position of Helios indicated by the five-pointed red star (**Figure**

411   **4c** and **Supplementary Figures 3c** and **4c** ). In particular, on 10 February 2023, when Helios

412   reached its climax, the maps in **Figure 4c** (SM) and **Supplementary Figures 3c** and **4c** (PM

413   and SPSM respectively) show a cluster of high RMS values for the stations installed near the

414  sub-tropical system Helios, highlighting a good match between the SM, SPSM, PM and Helios

415  positions.

416  Comparing the RMS amplitude time series obtained for the sub-tropical system Helios with

417  those obtained for the Medicane Apollo (Borzì et al., 2022), we observe a similar trend for the

418  SM and SPSM bands and a different behavior for the PM band. In particular, during the

419  Medicane Apollo, the analysis showed a significant amplitude increase for the SM and SPSM

420  bands while no significant changes for the PM band were observed. Instead, during the sub-

421  tropical system Helios, the RMS amplitude time series for the PM (**Supplementary Figure 2**),

422  although with two orders of magnitude smaller, showed a trend similar to the SM (**Figure 3**)

423  and SPSM (**Supplementary Figure 1**) ones. Also the space-time distribution shows a good

424  match between the PM (**Supplementary Figure 3**) and Helios position (**Figure 1**, **4c** and

425  **Supplementary Figures 3c** and **4c**), even if for this band there are stations installed in central

426  Italy that show high RMS amplitude values related to a very local storm surge that occurred at

427  the same time as Helios.

428  The involvement of the PM band in the case of the sub-tropical system Helios can be explained

429  by considering the position of this low-pressure system (**Figure 1**) and comparing it with the

430  Apollo position. Indeed, the Medicane Apollo develops and moves in the Ionian Sea (**Figure**

431  **2**) in an area with a sea depth greater than 2000 m, while the sub-tropical system Helios

432  develops and moves largely in the Sicily Channel, a shallower sea with a depth that reaches a

433  maximum depth of 500 m b.s.l. and an average depth of 316 m b.s.l. In addition, the average

434  depth between Sicily and Malta is about 65 m b.s.l. As outlined in the literature (Bromirski et

435  al., 2005), the production of the PM is hindered in large water depths due to the attenuation of

436  pressure fluctuations, which generate the signal, as a result of depth-dependent amplitude

437  decay. More specifically, the PM is generated solely in depths less than half of the wavelength

438  (where $\lambda$ represents the wavelength of the oceanic waves generating the pressure fluctuations).

439  If we consider, for the Catania and Mazara areas, a mean waves period of 6.1 and 5.6 s and a

440  peak waves period of 9.7 and 9 s respectively (Agenzia per la Protezione dell'Ambiente e per

441  i Servizi Tecnici Dipartimento Tutela Acque Interne e Marine Servizio Mareografico - Atlante

442  delle onde nei mari italiani), by utilizing the correlation that connects period and wavelength

443  ($\lambda=gT^2/2\pi$ with g acceleration of gravity that is 9.8 m/s$^2$ and T the period of the waves;

444  Sarpkaya and Isaacson, 1981) we obtain a wavelength, for this part of the Mediterranean sea,

445  ranging between ∼45 m and ∼150 m. Considering these wavelengths, the shallow depth of the

446  Sicily Channel, especially in the Malta Channel where the average depth is about 65 m b.s.l.,

447  and the fact that the generation of the PM occurs only for depths less than ½ λ (Bromirski et

448  al., 2005), we can remark that the generation of the PM is possible in the Sicily Channel, while

449  can not occur in the Ionian Sea except in limited areas near the coastline. This is evident in our

450  analysis, and in particular in the RMS amplitude time series. Indeed in the sub-tropical system

451  Helios case, which occurred in the Sicily Channel, we can note a similar trend between the

452  three analyzed microseism bands (**Figure 3** and **Supplementary Figures 1** and **2**), while in the

453  case of the Medicane Apollo, that developed in the Ionian Sea (Borzì et al., 2022), we observe

454  an RMS amplitude increase only for the SM and SPSM bands and no significant variations in

455  the PM bands.

456  **4.3. Comparing the RMS amplitude with the SWH**

457  As mentioned before, microseism is a continuous seismic signal linked to the hydrosphere-

458  solid Earth energy transfer and, as demonstrated by several authors (e.g. Ardhuin et al., 2012;

459  Bromirski et al., 1999; Bromirski et al., 2005; Cutroneo et al., 2021; Ferretti et al., 2013, 2018),

460  the amplitude of this signal is strictly related to the sea state and in particular to the SWH. To

461  analyze the relationship between microseism and SWH, we plot in **Figure 9a** the RMS

462  amplitude time series for the station IWAV5 and the SWH time series derived from both HF

463  Radar (SWH-HF) and hindcast maps (SWH-Hind), and in **Figure 5** the results of the

464    correlation analysis between the RMS amplitude time series and the significant wave height

465    (the position of the seismic stations IWAV5, LINA, MSDA and CLTA and HF radar are

466    respectively shown in **Figure** 2a and **2c**). The sea state information provided by the Mazara del

467    Vallo buoy was not taken into account in this analysis because of the long distance between

468    this instrument and the cyclone eye. We chose stations IWAV5, LINA, MSDA and CLTA both

469    because they are some of the nearest stations to the cyclone eye and since these stations were

470    used for the seismic signature analysis. In addition, as it is possible to see in **Figure 3a, b** and

471    **c**, all the seismic stations installed in the Sicily Channel area show very similar microseism

472    amplitude patterns. The time series of SWH-Hind was obtained by computing the median value

473    of the SWH data within a wide area of the Sicily Channel shown in **Figure 9d**. In general, the

474    three datasets exhibit a good agreement among them. In particular, we observe an increase that

475    occurs almost simultaneously for SWH-HF, SWH-Hind and the RMS amplitude. However,

476    from the first hours of 10 February, the SWH-HF started showing a different behavior

477    compared to SWH-Hind; indeed, the SWH-HF decreased while the SWH-Hind continued to

478    show high values up to the end of 10 February. This difference can be explained by considering

479    that the HF Radar provides information about the SWH for a limited area while SWH-Hind

480    gives median information about a wide area of the Sicily Channel. It is interesting to note that

481    the microseism amplitude follows more closely the areal sea state, shown by the SWH-Hind

482    series, than the punctual one, shown by the SWH-HF. We can note this in both a qualitative

483    way in the time series of **Figure 9a** and a quantitative way in the cross-plots of **Figures 9b** and

484    **c**. For both the cross-plots we calculated the $R^2$ value, to evaluate the goodness of the linear

485    regression, and we obtain $R^2$ values equal to 0.68 and 0.85, for the cross-plot RMS amplitude

486    vs SWH-HF and RMS amplitude vs SWH-Hind, respectively. The higher value of $R^2$ for the

487    RMS amplitude - SWH-Hind relationship can be explained by considering that microseism

488    recorded by a seismic station is generated by multiple extended sources distributed on a wide

489 portion of the sea. The correlation analysis confirms a good match between the spatial

490 distributions of SWH and RMS amplitudes recorded by the 4 aforementioned stations during

491 the period under investigation (**Figure 5**). Values of the correlation factor higher than 0.85

492 were observed for the SM and SPSM bands for the area of the Sicily Channel and Ionian Sea

493 affected by the storm surge due to the cyclone Helios.

494

495 **4.4. Localization analysis**

496 As concerns the microseism source location, we performed the location analysis for the PM,

497 SM and SPSM using both the array techniques and the grid search method based on the seismic

498 amplitude decay. Concerning the array techniques, we chose to focus on PM and SM bands

499 since, according to the information from the ARF, we expect reliable localizations only for

500 these two bands, while for the SPSM band appears spatial aliasing. As for the grid search

501 method, we obtained reliable locations only for the SM and SPSM bands, while for the PM

502 band, although we got localizations in agreement with the cyclone position, the associated $R^2$

503 values turned out to be slightly lower than the threshold from which we can consider the

504 locations reliable.

505 By the grid search method, we obtained reliable locations from 9 February 2023 at 8:00 to 11

506 February 2023 at 00:00 (**Supplementary figure 7**). In agreement with satellite images (**Figure**

507 **1**), on 9 February 2023, the sub-tropical system Helios was not yet well-developed and did not

508 show the cyclone eye. Indeed, during this day, we are able to locate a storm surge, probably

509 linked to the primitive formation of Helios, that occurred in the Ionian Sea. In particular, our

510 localizations, on 9 February from 8:00 to 20:00, indicate the source position near to the south-

511 eastern part of Sicily in agreement with the hindcast data showing for this area SWH greater

512 than 5 meters (**Figure 4b and 7**). During the following hours, our localizations

513 (**Supplementary figure 7**) show a small but continuous shift of the source toward the Malta

514      area (**Figure 6**), in agreement with the relatively stable position of the cyclone eye for the first

515      hours of 10 February 2023, retrieved from SEVIRI data (**Figure 1**). Successively, the sub-

516      tropical system rapidly loses its strength and runs out completely on the day of 11 February

517      2023, making landfall against the Libyan coast. The errors associated with the localization

518      show an anti-correlation with the $R^2$ (**Supplementary Figure 5**). In particular, we can observe

519      errors that vary from 535 to 210 km for the longitude and from 245 to 165 km for the latitude

520      In particular, we obtained lower errors during the climax of Helios, when the $R^2$ reached the

521      highest values, and higher during the initial and final phases of the phenomenon

522      (**Supplementary Figure 5 and Table 1**).

523      In **Table 1** we summarised the main features of the microseism source located by using the

524      grid search method during the days 9-10 February 2023 and compared these with the results

525      obtained during the period 01:00 - 23:00 of 10 February 2023 in terms of the coordinates of the

526      cyclone eye retrieved by SEVIRI data. During the first hours of the cyclone life, the coordinates

527      of the cyclone eye and the microseism source show only a small offset that, as explained in

528      section 3.4.1, can be due to the fact that the point-like microseism source corresponds with the

529      barycentric position of an extended source and it is expected that the microseism source

530      location could differ from the cyclone eye. During the following hours, as shown in **Figure 1,**

531      the cyclone moved southward until the time when the cyclone made landfall against the Libyan

532      coast. This shift is not visible in the microseism location results, probably due to the lack of

533      seismic stations in Africa, that would help locate more accurately seismic sources placed close

534      to the African Coastlines. In **Supplementary figure 8** we plot the temporal distribution of the

535      $R^2$ values and compare this with the SWH-Hind time series. These two datasets show a good

536      agreement and highlight that the higher $R^2$ values obtained from the grid search method are

537      influenced by the presence of the sub-tropical system Helios.

538    Concerning the array analysis, the result obtained for the PM band shows that, for the period

539    9-11 February, the back azimuth values pointed toward the Ionian Sea (**Supplementary figure**

540    **9**) with apparent velocity values of ~ 3.0 km/s (**Supplementary figure 10**). For the same days,

541    the back azimuth values for the SM band pointed toward the same region (**Supplementary**

542    **figure 11**), with apparent velocity values of ~ 2.0 km/s (**Supplementary figure 12**).

543    For the PM and the SPSM bands, we obtained reliable locations only by one of the two used

544    methods (array technique for the PM and grid search method for the SPSM), while for the SM

545    we obtained reliable locations from both the aforementioned methods and we can compare the

546    results obtained independently from these two methods. We can observe that the grid search

547    method based on the seismic amplitude decay is able to detect both the storm surge that

548    occurred in the Ionian sea and the following formation of the sub-tropical system Helios

549    (**Supplementary figure 7**), and in particular by this method, we localize the cyclone as a point-

550    like source, considered as a  barycentre of an extended source. The array technique instead

551    provides back azimuth values pointing toward the Ionian Sea for the entire period of 9-11

552    February (**Supplementary figure 11**). From these results, we can note that the two methods

553    are influenced by different sources. This different result can be explained based on  the spatial

554    station distribution. Indeed, if we consider the grid search method we use a wide station

555    network including stations installed near the sub-tropical system Helios (MSDA, CLTA,

556    IWAV5, LINA and other stations), while the Etnean array includes 15 stations clustered in a

557    small area. In addition, the distance array center-Ionian Sea (~20 km) is smaller than the

558    distance array center-Sicily Channel (~90 km). During the period taken into account, we have

559    the coexistence of two strength sources, the first in the Ionian Sea (storm surge with SWH

560    greater than 5 m) and the other, probably the strongest, in the Sicily Channel (Helios), both

561    represented by the red contour line in **Figure 4c**. Hence, the coexistence of two sources and

562    the great difference in distance between the array center and the Ionian Sea and the array center

563   and the Sicily channel does not allow us to locate the sub-tropical system Helios with the array

564   technique, which gives us back azimuth values pointing always toward the nearest source.

**4.5. Seismic signature**

566   To show the main spectral characteristics of the sub-tropical system Helios, we used the method

567   developed by Soubestre et al. (2018). From our analysis, the evolution in time of the

568   microseism spectral characteristics between the first 24 hours and the following ones is evident

569   (**Figure 10**). In particular, with the vertical dashed lines in **Figure 10,** we show the time interval

570   when Helios develops, reaches the climax and loses power to run out. The first 24 hours are

571   characterized by the lack of a clear predominance of a particular frequency range. Starting from

572   early 9 February 2023 (first vertical white dashed line), we can observe high coherence values

573   clustered on a narrow frequency range between about 0.14 and 0.25 Hz, and this frequency

574   range is constant until the 80 hours (vertical black dashed line) corresponding to the morning

575   of 11 February. Successively, the frequency with the highest coherence starts to increase

576   reaching a value of about 0.35 Hz before the exhaustion of the phenomenon. This increase in

577   the frequency could be related to the landfall of Helios against the Lybian coast

578   (https://twitter.com/medcyclones/status/1624143740800536591?s=20, last access 23/05/2023

579   ). Indeed, as described in the literature (Gerstof et al., 2006; Lin et al., 2017; Sun et al., 2013),

580   there exists a relationship between the frequency, the sea depth and the development of local

581   wave motion near the coastline. In particular, Gerstof et al. (2006) show an increase in the

582   microseism frequency during the two landfalls of Hurricane Katrina. Similar results are shown

583   by Sun et al. (2013), who highlighted an increase in the intensity of the microseism for the SM

584   and SPSM and the frequency increase from the SM band toward the SPSM one during the

585   approaching of the three analyzed typhoons against the Chinese coast. Finally, Lin et al. (2017)

586   show an increase in the microseism frequency during the first landfall of typhoon Megi.

587   Similarly, we obtained an increase in frequency during the time interval when Helios

approached the Lybian coastline and made landfall on 11 February (https://twitter.com/medcyclones/status/1624143740800536591?s=20, last access 23/05/2023). We were also able to observe the gradual loss of power of the sub-tropical system highlighted by ever-lower coherence values until its disappearance.

**5. Conclusions**

Several works have dealt with the relationship between microseism and several meteorological phenomena, considering in particular storm surges (Ardhuin et al., 2019; Cannata et al., 2020; Guerin et al., 2022; Moschella et al., 2020) and different types of cyclones (Borzì et al., 2022; Bromirski, 2001; Bromirski et al., 2005; Gerstoft et al., 2006; Gualtieri et al., 2018; Lin et al., 2017; Retailleau and Gualtieri, 2019, 2021; Zhang et al., 2010) that affect various parts of the world (hurricanes, typhoons, tropical cyclones and medicanes). In this work, we analyzed the relationship between the three main microseism bands (PM, SM and SPSM) and the sub-tropical system Helios that occurred in the Mediterranean Sea during the time interval 9-11 February 2023. Although all the meteorological parameters suggest that Helios has not been able to reach the fully Medicane characteristics, remaining a rather weak sub-tropical system, the proximity of this cyclone to the southeastern Sicilian and Maltese coastal area has caused heavy rainfall, strong wind gusts and violent storm surge in the two above mentioned areas.

To obtain information about the sea state we take into account the data of hindcast maps, wavemeter buoy, HF radar and SEVIRI images. The first three methodologies show an increase in the SWH during the period under investigation, with a climax during the days 9-10 February 2023, due to the presence of the sub-tropical system Helios. In particular, the HF radar and the hindcast maps exhibit an SWH of about 6 meters while the wavemeter buoy shows an SWH of about 3 meters. This difference is only linked to the position where the two instruments are installed, indeed the HF radar is installed at about 90 km from the cyclone eye while the wavemeter buoy is installed at about 190 km. The last method based on SEVIRI images provide

613   information about the location of the cyclone eye that is clearly visible between 01:00 and

614   23:00 on 10 February 2023.

615   To analyze this meteorological phenomenon from a seismic point of view, we selected 120

616   seismic stations installed along the Italian, Maltese and Greek coastal areas: i) 105 were used

617   in spectral and amplitude analysis, in the grid search method and 4 of these to obtain the seismic

618   signature of Helios using the method of the covariance matrix; ii) 15 were employed in array

619   analysis. The results, obtained from the spectral analysis, highlight that the seismic signals, in

620   particular the PM, SM and SPSM bands, are affected by the storm surge and by the sub-tropical

621   system Helios. This is evident considering the RMS amplitude time series, the spectrograms

622   and the RMS amplitude space-time distribution, in which it is possible to observe that the

623   amplitude of the microseism signal, in the three main bands above mentioned, shows a similar

624   trend and it is greater during the period 9-10 February 2023 for the stations installed close to

625   the Sicily Channel (for example the stations MSDA, LINA and IWAV5), while the stations

626   installed farther from Helios (for example CELB) show a different behavior conditioned by

627   local sources. Furthermore, the increase of the RMS amplitude for the PM band can be

628   explained on the basis of the position where Helios develops. Indeed, as explained in the

629   literature (Bromirski et al., 2005), the generation of the PM is limited in the areas where the

630   depth of the sea bottom is smaller than $\frac{1}{2}\lambda$ (where $\lambda$ is the wavelength of the sea waves) as a

631   consequence of the amplitude decay of the pressure fluctuations. The Sicily Channel and in

632   particular the area between Malta and Sicily (Malta Channel), where Helios stood still for the

633   entire 10 February 2023, shows an average depth of about 65 m b.s.l., and considering

634   wavelength between ∼45 m and ∼150 m it is possible the generation of the PM for this area.

635   By comparing the SWH recorded by HF Radar, SWH retrieved by hindcast data and the RMS

636   amplitude recorded at the station IWAV5, we observe that the RMS amplitude time series

637   shows a trend more similar to that of hindcast data than to the HF Radar data. This could be

explained by considering that the microseism is a seismic signal generated by multiple and extended sources in a large area of the sea and hence its amplitude is related to the state of a wide portion of the sea. Also, the correlation analysis confirms a good match between the spatial distributions of significant wave heights and seismic RMS amplitudes.

We used two different methods to track the position of the sub-tropical system Helios during its lifetime and, through the performed analysis, we were able to locate both the storm surge that occurred in the Ionian Sea and Helios. In particular, using the grid search method based on the seismic amplitude decay we located the storm surge in the Ionian Sea on 9 February 2023 and the sub-tropical system Helios on the next day, while with the array technique, we located only the storm surge in the Ionian Sea as a consequence of the position of the array closer to the Ionian Sea than to the Sicily Channel. The location obtained both for the storm surge and for the sub-tropical system Helios, during the first hours of its life, is in agreement with the real position of the two meteorological phenomena shown by the hindcast maps and satellite images. Successively, the sub-topical system Helios moved southward until the time when the cyclone made landfall against the Libyan coast while the microseism source continued to show a stable position near Malta Island. This difference between the two positions is probably due to the lack of seismic stations in Africa, that does not locate accurately microseism sources placed close to the African Coastlines. In addition, using the method of the covariance matrix, we obtained the seismic signature of the sub-tropical system Helios. In particular, during the development and climax of the cyclone Helios, we can observe high coherence values clustered on a narrow frequency range between about 0.14 and 0.25 Hz that, as described in the literature, corresponds to the microseism bands (SM and SPSM) most affected by cyclonic activity. This narrow frequency range stays constant until the time when Helios makes landfall when we observe an increase in the frequency until a value of about 0.35 Hz probably linked to the decrease of the sea depth and the development of local wave motion near the coastline.

Starting from Borzì et al. (2022), this work aims at studying and monitoring the Mediterranean cyclones through microseism and its integration with sea state data. It underlines that it is possible to extract information about these meteorological phenomena by an innovative system for the sea state monitoring that includes not only the classical instruments (such as wavemeter buoys, radar HF and geostationary satellites) but also seismometers. In particular, the large number of broadband seismic stations, installed for earthquake and volcanic monitoring, can compensate for the lack of data of the classical instruments mentioned above, more often affected by instrument breakage.

Finally, since we obtained the seismic signature of this particular Mediterranean cyclone we can compare it with the seismic signature of other Mediterranean events (Medicane and common storms) to identify the similarities and differences in the spectral content of different Mediterranean cyclones and other more common events. The characterization of the seismic signature of these events could be useful to identify Mediterranean cyclones by old seismograms, and hence to reconstruct the temporal variability (in terms of occurrence rate and intensity) of these extreme meteo-marine events whose evolution seems to be strictly linked to the global warming (e.g. Emanuel, 2005; Reguero et al., 2019).

**Data availability**

The seismic data, in the miniseed format used in this study, can be downloaded through the ORFEUS-EIDA database (http://www.orfeus-eu.org/data/eida/). All the seismic stations used in this study, along with their main features, are reported in Supplementary Tables 1 and 2. The hindcast data are available online on the Copernicus site (https://resources.marine.copernicus.eu/products). The Italian buoy data (Mazara del Vallo) are available on the ISPRA website (https://dati.isprambiente.it/) and on the MAREOGRAFICO

688 website (www.mareografico.it). Satellite data are available on the EUMETSAT website

689 (https://navigator.eumetsat.int/product/EO:EUM:DAT:MSG:HRSEVIRI). The HF Radar data

690 are available on the CALYPSO project website by compiling the form indicated on the web

691 page (https://www.calypsosouth.eu/index.php/welcome/open_page/50/0) or by contacting

692 giuseppe.ciraolo@unipa.it or salvatore.aronica@cnr.it.

693 **Acknowledgments**

694 The authors thank the i-waveNET "Implementation of an innovative system for monitoring the

695 state of the sea in climate change scenarios" project, funded by the Interreg Italia-Malta

696 Programme (https://iwavenet.eu/; notice 2/2019 Axis 3; project code C2-3.2-106) and the

697 ARCHIMEDE "MultidisciplinARy approaCH to better define vulnerabIlity and hazard of

698 MEDicanEs along the Ionian coasts of Sicily" project (code P2022MJKMA). We also thank

699 the grant PIACERI, 2020-22 programme: PAROSSISMA project (code 22722132140,

700 principal investigator Marco Viccaro) and Open Access. A.M.B. thanks the PON "Ricerca e

701 Innovazione 2014-2020 Azione IV.5 – Dottorati su tematiche green". The authors are grateful

702 to Prof. Vittorio Scribano, the Museo Archeologico di Kamarina, Parco di Kamarina e Cava

703 D'Ispica - Direttore Arch. Domenico Buzzone and the Centro Polifunzionale di Protezione

704 Civile – Dott.ssa Emilia Pluchinotta, for hosting the seismic stations installed in the framework

705 of the i-waveNET project and used in this work (IWAV2, IWAV3, IWAV3). This study has

706 been conducted using E.U. Copernicus Marine Service Information,

707 https://doi.org/10.25423/cmcc/medsea_multiyear_wav_006_012. The seismic data,

708 downloaded using the EIDA and ORFEUS webservices, belong to the AC, FR, HC, HL, HP,

709 IV, ML and MN networks. T.L. and R.D.P. thank the research project "SEISMOSTORM"

710 funded by the BRAIN-be 2 program of the Federal Science Policy (BELSPO). We thank the

711 handling editor Jiping Xie,and the anonymous reviewers for comments that helped clarify our

712 paper.

713

714

715  **References**

716

717  ● Agenzia per la Protezione dell'Ambiente e per i Servizi Tecnici Dipartimento Tutela

718  Acque Interne e Marine Servizio Mareografico - Atlante delle onde nei mari italiani -

719  Università degli studi di Roma Tre

720  http://opac.apat.it/sebina/repository/catalogazione/immagini/pdf/atlante%20mari%201

721  _60_2_.pdf

722  ● Androulidakis, Y., Makris, C., Mallios, Z., Pytharoulis, I., Baltikas, V., & Krestenitis,

723  Y. Storm surges during a Medicane in the Ionian Sea. *Proceedings of the Marine and*

724  *Inland Waters Research Symposium, Porto Heli, Greece*. p. 16-19, 2022..

725  ● Ardhuin, F., & Roland, A. "Coastal wave reflection, directional spread, and

726  seismoacoustic noise sources." *Journal of Geophysical Research: Oceans* 117.C11,

727  2012.

728  ● Ardhuin, F.; Gualtieri, L.; Stutzmann, E. How ocean waves rock the Earth: Two

729  mechanisms explain microseisms with periods 3 to 300 s. *Geophysical Research*

730  *Letters*, 42.3: 765-772, https://doi.org/10.1002/2014GL062782, 2015.

731  ● Ardhuin, F., Stopa, J. E., Chapron, B., Collard, F., Husson, R., Jensen, R. E., ... &

732  Young, I. Observing sea states. *Frontiers in Marine Science*, 124,

733  https://doi.org/10.3389/fmars.2019.00124, 2019.

734  ● Battaglia, J., & Aki, K. Location of seismic events and eruptive fissures on the Piton de

735  la Fournaise volcano using seismic amplitudes. *Journal of Geophysical Research: Solid*

736  *Earth*, *108*(B8), https://doi.org/10.1029/2002JB002193, 2003.

737  ● Battaglia, J., Aki, K., & Ferrazzini, V. Location of tremor sources and estimation of

738  lava output using tremor source amplitude on the Piton de la Fournaise volcano: 1.

739        Location of tremor sources. Journal of volcanology and geothermal research, 147(3-4),

740        268-290, https://doi.org/10.1016/j.jvolgeores.2005.04.005, 2005.

741    ● Bencivenga, M., Nardone, G., Ruggiero, F., & Calore, D., The Italian Data Buoy

742        Network. *WTI Trans. Eng. Sci.*, 74, 321–332, 2012.

743    ● Borzì, A. M., Minio, V., Cannavò, F., Cavallaro, A., D'Amico, S., Gauci, A., ... &

744        Cannata, A. Monitoring extreme meteo-marine events in the Mediterranean area using

745        the microseism (Medicane Apollo case study). *Scientific Reports*, *12*(1), 21363,

746        https://doi.org/10.1038/s41598-022-25395-9, 2022.

747    ● Bouin, M. N., & Lebeaupin Brossier, C. Surface processes in the 7 November 2014

748        medicane from air–sea coupled high-resolution numerical modelling. *Atmospheric*

749        *Chemistry and Physics*, *20*(11), 6861-6881, 2020.

750    ● Bromirski, Peter D., Reinhard E. Flick, and Nicholas Graham. "Ocean wave height

751        determined from inland seismometer data: Implications for investigating wave climate

752        changes in the NE Pacific." *Journal of Geophysical Research: Oceans* 104.C9 20753-

753        20766, https://doi.org/10.1029/1999JC900156, 1999.

754    ● Bromirski, Peter D. "Vibrations from the "perfect storm"." *Geochemistry, Geophysics,*

755        *Geosystems* 2.7, https://doi.org/10.1029/2000GC000119, 2001.

756    ● Bromirski, Peter D., Fred K. Duennebier, and Ralph A. Stephen. "Mid-ocean

757        microseisms." *Geochemistry, Geophysics, Geosystems* 6.4,

758        https://doi.org/10.1029/2004GC000768, 2005.

759    ● Cannata, A., Di Grazia, G., Aliotta, M., Cassisi, C., Montalto, P., & Patanè, D.

760        Monitoring seismo-volcanic and infrasonic signals at volcanoes: Mt. Etna case study.

761        *Pure and Applied Geophysics*, *170*, 1751-1771, https://doi.org/10.1007/s00024-012-

762        0634-x, 2013.

763 ● Cannata, A., Cannavò, F., Moschella, S., Di Grazia, G., Nardone, G., Orasi, A., ... &

764 Gresta, S. Unravelling the relationship between microseisms and spatial distribution of

765 sea wave height by statistical and machine learning approaches. *Remote Sensing*, *12*(5),

766 761, https://doi.org/10.3390/rs12050761, 2020.

767 ● Carrió, D. S., Homar, V., Jansa, A., Romero, R., & Picornell, M. A. Tropicalization

768 process of the 7 November 2014 Mediterranean cyclone: Numerical sensitivity study.

769 *Atmospheric Research*, *197*, 300-312, https://doi.org/10.1016/j.atmosres.2017.07.018,

770 2017.

771 ● Capodici, F., Cosoli, S., Ciraolo, G., Nasello, C., Maltese, A., Poulain, P. M., ... &

772 Gauci, A. Validation of HF radar sea surface currents in the Malta-Sicily Channel.

773 *Remote sensing of environment*, *225*, 65-76, https://doi.org/10.1016/j.rse.2019.02.026,

774 2019.

775 ● Cavicchia, Leone, Hans von Storch, and Silvio Gualdi. "Mediterranean tropical-like

776 cyclones in present and future climate." *Journal of Climate* 27.19, 7493-7501,

777 https://doi.org/10.1175/JCLI-D-14-00339.1, 2014.

778 ● Comellas Prat, A., Federico, S., Torcasio, R. C., D'Adderio, L. P., Dietrich, S., &

779 Panegrossi, G. Evaluation of the sensitivity of medicane Ianos to model microphysics

780 and initial conditions using satellite measurements. *Remote Sensing*, *13*(24), 4984,

781 https://doi.org/10.3390/rs13244984, 2021.

782 ● Cutroneo, L., Ferretti, G., Barani, S., Scafidi, D., De Leo, F., Besio, G., & Capello, M..

783 Near real-time monitoring of significant sea wave height through microseism

784 recordings: Analysis of an exceptional sea storm event. *Journal of Marine Science and*

785 *Engineering*, *9*(3), 319, https://doi.org/10.3390/jmse9030319, 2021.

786    ● D'Adderio, L. P., Panegrossi, G., Dafis, S., Rysman, J. F., Casella, D., Sanò, P., ... &
787       Miglietta, M. M. Helios and Juliette: Two Falsely Acclaimed Medicanes. *Available at*
788       *SSRN 4542818*.

789    ● Dafis, S., Rysman, J. F., Claud, C., & Flaounas, E. Remote sensing of deep convection
790       within a tropical-like cyclone over the Mediterranean Sea. *Atmospheric Science Letters*,
791       *19*(6), e823, https://doi.org/10.1002/asl.823,  2018.

792    ● Davies R. Cyclone Helios, Malta and Italy, February 2023,
793       https://www.efas.eu/en/news/cyclone-helios-malta-and-italy-february-2023,      last
794       access 13/04/2023)

795    ● Delibera      di      Giunta      -      Regione      Siciliana
796       (https://www2.regione.sicilia.it/delibereregiunta/file/giunta/allegati/N.099_15.02.2023.p
797       df, last access 13/04/2023)

798    ● Di Muzio, E., Riemer, M., Fink, A. H., & Maier-Gerber, M. Assessing the predictability
799       of Medicanes in ECMWF ensemble forecasts using an object-based approach.
800       *Quarterly Journal of the Royal Meteorological Society*, *145*(720), 1202-1217,
801       https://doi.org/10.1002/qj.3489, 2019.

802    ● Emanuel, K. Increasing destructiveness of tropical cyclones over the past 30 years.
803       *Nature*, *436*(7051), 686-688, https://doi.org/10.1038/nature03906, 2005.

804    ● Faranda, D., Bourdin, S., Ginesta, M., Krouma, M., Noyelle, R., Pons, F., ... & Messori,
805       G. A climate-change attribution retrospective of some impactful weather extremes of
806       2021. *Weather and Climate Dynamics*, *3*(4), 1311-1340, https://doi.org/10.5194/wcd-
807       3-1311-2022, 2022.

808    ● Ferretti, G., Zunino, A., Scafidi, D., Barani, S., & Spallarossa, D. On microseisms
809       recorded near the Ligurian coast (Italy) and their relationship with sea wave height.

810    *Geophysical        Journal        International*,        *194*(1),        524-533,

811        https://doi.org/10.1093/gji/ggt114,  2013.

812    ● Ferretti, G., Barani, S., Scafidi, D., Capello, M., Cutroneo, L., Vagge, G., & Besio, G.

813        Near real-time monitoring of significant sea wave height through microseism

814        recordings: An application in the Ligurian Sea (Italy). *Ocean & Coastal Management*,

815        *165*, 185-194, https://doi.org/10.3390/jmse9030319, 2018.

816    ● Flaounas, E., Davolio, S., Raveh-Rubin, S., Pantillon, F., Miglietta, M. M., Gaertner,

817        M. A., ... & Ricard, D. Mediterranean cyclones: Current knowledge and open questions

818        on dynamics, prediction, climatology and impacts. *Weather and Climate Dynamics*,

819        *3*(1), 173-208, https://doi.org/10.5194/wcd-3-173-2022, 2022.

820    ● Gerstoft, P., Fehler, M. C., & Sabra, K. G. When katrina hit california. *Geophysical*

821        *Research Letters*, *33*(17), https://doi.org/10.1029/2006GL027270,  2006.

822    ● Gualtieri, L., Camargo, S. J., Pascale, S., Pons, F. M., & Ekström, G. The persistent

823        signature of tropical cyclones in ambient seismic noise. *Earth and Planetary Science*

824        *Letters*, *484*, 287-294, https://doi.org/10.1016/j.epsl.2017.12.026, 2018.

825    ● Guerin, G., Rivet, D., Van Den Ende, M. P. A., Stutzmann, E., Sladen, A., & Ampuero,

826        J. P. Quantifying microseismic noise generation from coastal reflection of gravity

827        waves recorded by seafloor DAS. *Geophysical Journal International*, *231*(1), 394-407,

828        https://doi.org/10.1093/gji/ggac200,  2022.

829    ● Johnson, R. W. (2001). An introduction to the bootstrap. Teaching statistics, 23(2), 49-

830        54.

831    ● Hart, R. E. A cyclone phase space derived from thermal wind and thermal asymmetry.

832        *Monthly    weather    review*,    *131*(4),    585-616,    https://doi.org/10.1175/1520-

833        0493(2003)131%3C0585:ACPSDF%3E2.0.CO;2, 2003.

- Hasselmann, Klaus. "A statistical analysis of the generation of microseisms." *Reviews of Geophysics* 1.2, 177-210, 1963.

- Haubrich, Richard A., and Keith McCamy. "Microseisms: Coastal and pelagic sources." *Reviews of Geophysics* 7.3: 539-571, 1969.

- Kerkmann J. and Bachmeier S. Development of a tropical storm in the Mediterranean Sea (6–9 November 2011). Available at: https://www.eumetsat.int/tropical-storm-develops-mediterranean-sea (last access: 15 February 2023), 2011.

- Korres, G., Ravdas, M., & Zacharioudaki, A. Mediterranean Sea Waves Hindcast (CMEMS MED-Waves) [Data set]. Copernicus Monitoring Environment Marine Service (CMEMS). https://doi.org/10.25423/CMCC/MEDSEA_HINDCAST_WAV_006_012, 2019

- Kumagai, H., Placios, P., Ruiz, M., Yepes, H., & Kozono, T. Ascending seismic source during an explosive eruption at Tungurahua volcano, Ecuador. *Geophysical Research Letters*, *38*(1), https://doi.org/10.1029/2010GL045944, 2011.

- Lagouvardos, K., Karagiannidis, A., Dafis, S., Kalimeris, A., & Kotroni, V. Ianos—A hurricane in the Mediterranean. *Bulletin of the American Meteorological Society*, *103*(6), E1621-E1636, https://doi.org/10.1175/BAMS-D-20-0274.1, 2022.

- Lepore,S and Grad, M. "Analysis of the primary and secondary microseisms in the wavefield of the ambient noise recorded in northern Poland." *Acta Geophysica*: 66, 915-929 , 2018.

- Lin, J., Lin, J., & Xu, M. Microseisms generated by super typhoon Megi in the western Pacific Ocean. *Journal of Geophysical Research: Oceans*, *122*(12), 9518-9529, https://doi.org/10.1002/2017JC013310, 2017.

- Lionello, P., Conte, D., & Reale, M. The effect of cyclones crossing the Mediterranean region on sea level anomalies on the Mediterranean Sea coast. *Natural Hazards and*

859   *Earth System Sciences*, *19*(7), 1541-1564, https://doi.org/10.5194/nhess-19-1541-2019,
860   2019.

861   ● Long, R. M., Barrick, D., Largier, J. L., & Garfield, N. Wave observations from central
862   California: SeaSonde systems and in situ wave buoys. *Journal of Sensors*,
863   https://doi.org/10.1155/2011/728936, *2011*.

864   ● Longuet-Higgins, Michael Selwyn. "A theory of the origin of microseisms."
865   *Philosophical Transactions of the Royal Society of London. Series A, Mathematical and*
866   *Physical Sciences* 243.857, 1-35, 1950.

867   ● Lorente, P., Lin-Ye, J., Garcia-Leon, M., Reyes, E., Fernandes, M., Sotillo, M. G., ...
868   & Alvarez-Fanjul, E. On the performance of high frequency radar in the western
869   mediterranean during the record-breaking storm gloria. *Frontiers in Marine Science*, *8*,
870   645762, https://doi.org/10.3389/fmars.2021.645762, 2021.

871   ● Miglietta, M. M., Moscatello, A., Conte, D., Mannarini, G., Lacorata, G., & Rotunno,
872   R. Numerical analysis of a Mediterranean 'hurricane' over south-eastern Italy:
873   Sensitivity experiments to sea surface temperature. *Atmospheric research*, *101*(1-2),
874   412-426, https://doi.org/10.1016/j.atmosres.2011.04.006, 2011.

875   ● Miglietta, M. M., Laviola, S., Malvaldi, A., Conte, D., Levizzani, V., & Price, C.
876   Analysis of tropical-like cyclones over the Mediterranean Sea through a combined
877   modeling and satellite approach. *Geophysical Research Letters*, *40*(10), 2400-2405,
878   https://doi.org/10.1002/grl.50432, 2013.

879   ● Miglietta, M. M., & Rotunno, R. Development mechanisms for Mediterranean tropical-
880   like cyclones (medicanes). *Quarterly Journal of the Royal Meteorological Society*,
881   *145*(721), 1444-1460, https://doi.org/10.1002/qj.3503, 2019.

882   ● Moschella, S., Cannata, A., Cannavò, F., Di Grazia, G., Nardone, G., Orasi, A., ... &
883   Gresta, S. Insights into microseism sources by array and machine learning techniques:

884    Ionian and Tyrrhenian sea case of study. *Frontiers in Earth Science*, *8*, 114,

885    https://doi.org/10.3389/feart.2020.00114, 2020.

886    ● Nastos, P. T., Papadimou, K. K., & Matsangouras, I. T. Mediterranean tropical-like

887    cyclones: Impacts and composite daily means and anomalies of synoptic patterns.

888    *Atmospheric Research*, *208*, 156-166, https://doi.org/10.1016/j.atmosres.2017.10.023,

889    2018.

890    ● Oliver, J., & Page, R. Concurrent storms of long and ultralong period microseisms.

891    *Bulletin of the Seismological Society of America*, *53*(1), 15-26, 1963.

892    ● Orasi, A., Picone, M., Drago, A., Capodici, F., Gauci, A., Nardone, G., ... & Alonso-

893    Martirena, A. HF radar for wind waves measurements in the Malta-Sicily Channel.

894    *Measurement*, *128*, 446-454, https://doi.org/10.1016/j.measurement.2018.06.060,

895    2018.

896    ● Pravia-Sarabia, E., Gómez-Navarro, J. J., Jiménez-Guerrero, P., & Montávez, J. P.

897    Influence of sea salt aerosols on the development of Mediterranean tropical-like

898    cyclones. *Atmospheric Chemistry and Physics*, *21*(17), 13353-13368,

899    https://doi.org/10.5194/acp-21-13353-2021, 2021.

900    ● Portmann, R., González-Alemán, J. J., Sprenger, M., & Wernli, H. How an uncertain

901    short-wave perturbation on the North Atlantic wave guide affects the forecast of an

902    intense Mediterranean cyclone (Medicane Zorbas). *Weather and Climate Dynamics*,

903    *1*(2), 597-615, https://doi.org/10.5194/wcd-1-597-2020,  2020.

904    ● Reguero, B. G., Losada, I. J., & Méndez, F. J. A recent increase in global wave power

905    as a consequence of oceanic warming. *Nature communications*, *10*(1), 205,

906    https://doi.org/10.1038/s41467-018-08066-0, 2019.

907 ● Retailleau, L., & Gualtieri, L. Toward high-resolution period-dependent seismic
908   monitoring of tropical cyclones. *Geophysical Research Letters*, *46*(3), 1329-1337,
909   https://doi.org/10.1029/2018GL080785, 2019.

910 ● Retailleau, L., & Gualtieri, L. Multi-phase seismic source imprint of tropical cyclones.
911   *Nature communications*, *12*(1), 2064, https://doi.org/10.1038/s41467-021-22231-y,
912   2021.

913 ● Rost, S., & Thomas, C. Array seismology: Methods and applications. *Reviews of*
914   *geophysics*, *40*(3), 2-1, https://doi.org/10.1029/2000RG000100, 2002.

915 ● Rumora, I., Jukić, O., Filić, M., & Filjar, R. A study of GPS positioning error associated
916   with tropospheric delay during Numa Mediterranean cyclone. *Int J for Transp and Traff*
917   *Eng*, *8*(3), 282-293, https://doi.org/10.7708/ijtte.2018.8(3).03,  2018.

918 ● Sarpkaya, T., & Isaacson, M. Mechanics of wave forces on offshore structures Van
919   Nostrand Reinhold Company New York. *New York,* 1981.

920 ● Saviano, S., Kalampokis, A., Zambianchi, E., & Uttieri, M. A year-long assessment of
921   wave measurements retrieved from an HF radar network in the Gulf of Naples
922   (Tyrrhenian Sea, Western Mediterranean Sea). *Journal of Operational Oceanography*,
923   *12*(1), 1-15, https://doi.org/10.1080/1755876X.2019.1565853,  2019.

924 ● Scardino, G., Scicchitano, G., Chirivì M., Costa P.J.M., Luparelli A., Mastronuzzi G.
925   Convolutional Neural Network and Optical Flow for the Assessment of Wave and Tide
926   Parameters from Video Analysis (LEUCOTEA): An Innovative Tool for Coastal
927   Monitoring. Remote Sensing, 14, 2994, doi.org/10.3390/rs14132994, 2022.

928 ● Scicchitano, G., Scardino, G., Monaco, C., Piscitelli, A., Milella, M., De Giosa, F., &
929   Mastronuzzi, G. Comparing impact effects of common storms and Medicanes along the
930   coast    of    south-eastern    Sicily.    *Marine    Geology*,    *439*,    106556,
931   https://doi.org/10.1016/j.margeo.2021.106556, 2021.

932     ●   Shaltout, M., & Omstedt, A. Recent sea surface temperature trends and future scenarios

933         for the Mediterranean Sea. *Oceanologia*, *56*(3), 411-443, https://doi.org/10.5697/oc.56-

934         3.411, 2014.

935     ●   Soubestre, J., Shapiro, N. M., Seydoux, L., de Rosny, J., Droznin, D. V., Droznina, S.

936         Y., ... & Gordeev, E. I. Network-based detection and classification of seismovolcanic

937         tremors: Example from the Klyuchevskoy volcanic group in Kamchatka. *Journal of*

938         *Geophysical Research: Solid Earth*, *123*(1), 564-582,

939         https://doi.org/10.1002/2017JB014726, 2018.

940     ●   Sun, T., Xue, M., Le, K. P., Zhang, Y., & Xu, H. Signatures of ocean storms on seismic

941         records in South China Sea and East China Sea. *Marine Geophysical Research*, *34*,

942         431-448, https://doi.org/10.1007/s11001-013-9204-6, 2013.

943     ●   Tous, M., & Romero, R. Meteorological environments associated with medicane

944         development. *International Journal of Climatology*, *33*(1), 1-14,

945         https://doi.org/10.1002/joc.3428, 2013.

946     ●   Trnkoczy, A., Bormann, P., Hanka, W., Holcomb, L. G., Nigbor, R. L., Shinohara, M.,

947         ... & Suyehiro, K. Site selection, preparation and installation of seismic stations. In *New*

948         *Manual of Seismological Observatory Practice 2 (NMSOP-2)* (pp. 1-139). Deutsches

949         GeoForschungsZentrum GFZ, 2012.

950     ●   Tweet                                            medcyclones:

951         https://twitter.com/medcyclones/status/1623795373423620096?s=20,

952         https://twitter.com/medcyclones/status/1623992335104081921?s=20,

953   https://twitter.com/medcyclones/status/1624143740800536591?s=20

954     ●   Varlas, G., Vervatis, V., Spyrou, C., Papadopoulou, E., Papadopoulos, A., &

955         Katsafados, P. Investigating the impact of atmosphere–wave–ocean interactions on a

956     Mediterranean tropical-like cyclone. *Ocean Modelling*, *153*, 101675,
957     https://doi.org/10.1016/j.ocemod.2020.101675, 2020.

958    ● Welch, P. D. The use of Fast Fourier Transform for the estimation of power spectra: a
959     method based on time averaging over short, modified periodograms, IEEE T. Audio
960     Electroacoust. 15, 70–73, https://doi.org/10.1109/TAU.1967.1161901, 1967.

961    ● Zhang, J., Gerstoft, P., & Bromirski, P. D. Pelagic and coastal sources of P-wave
962     microseisms: Generation under tropical cyclones. *Geophysical Research Letters*,
963     *37*(15), https://doi.org/10.1029/2010GL044288, 2010.

964    ● Zimbo, F., Ingemi, D., & Guidi, G. The tropical-like cyclone "ianos" in September
965     2020. *Meteorology*, *1*(1), 29-44, https://doi.org/10.3390/meteorology1010004, 2022.

966

967

968

969

970

**Authors Contribution**

A.M.B., A.C. and F.C. conceived the idea. A.M.B. analyzed seismic data and V.M. performed

array analysis. C.L.R, G.N., A.O. and M.P. analyzed buoys data. S.A., D.C., G.D.G., G.L.,

S.D., R.D. and T.L. helped perform seismic analysis. F.C., G.C., S.A., I.F., G.G. G.M.,

analyzed HF Radar Data. A.M.B. and V.M. wrote the paper. S.A., F.C., D.C., G.L. and V.M.

dealt with the new seismic installation. G.C. lead one of the projects funding this research, G.S.

helped to interpret the sea state data. All the authors discussed the results, edited the paper and

gave consent for this publication under the supervision of A.C.

979

980

981

**Figures**

983
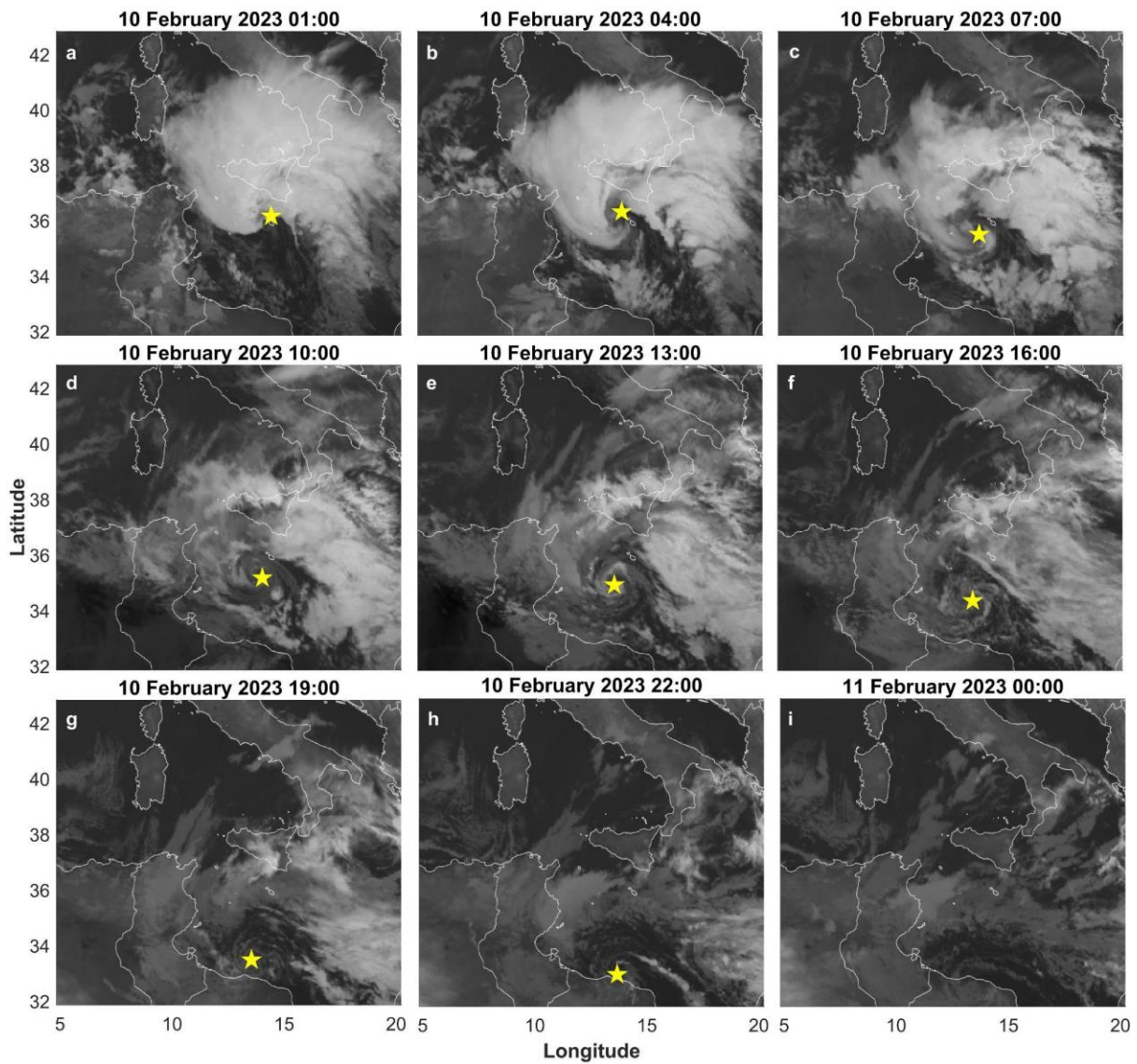
**Figure 1:** Satellite images of the Mediterranean area and of the sub-tropical system Helios during the period 10/02/2023 01:00 - 11/02/2023 00:00. The yellow stars in (a-h) show the position of the cyclone eye. The lack of the star in (i) is due to the dissipation of Helios after the landfall against the Libyan coast (h). (©EUMETSAT SEVIRI Images)
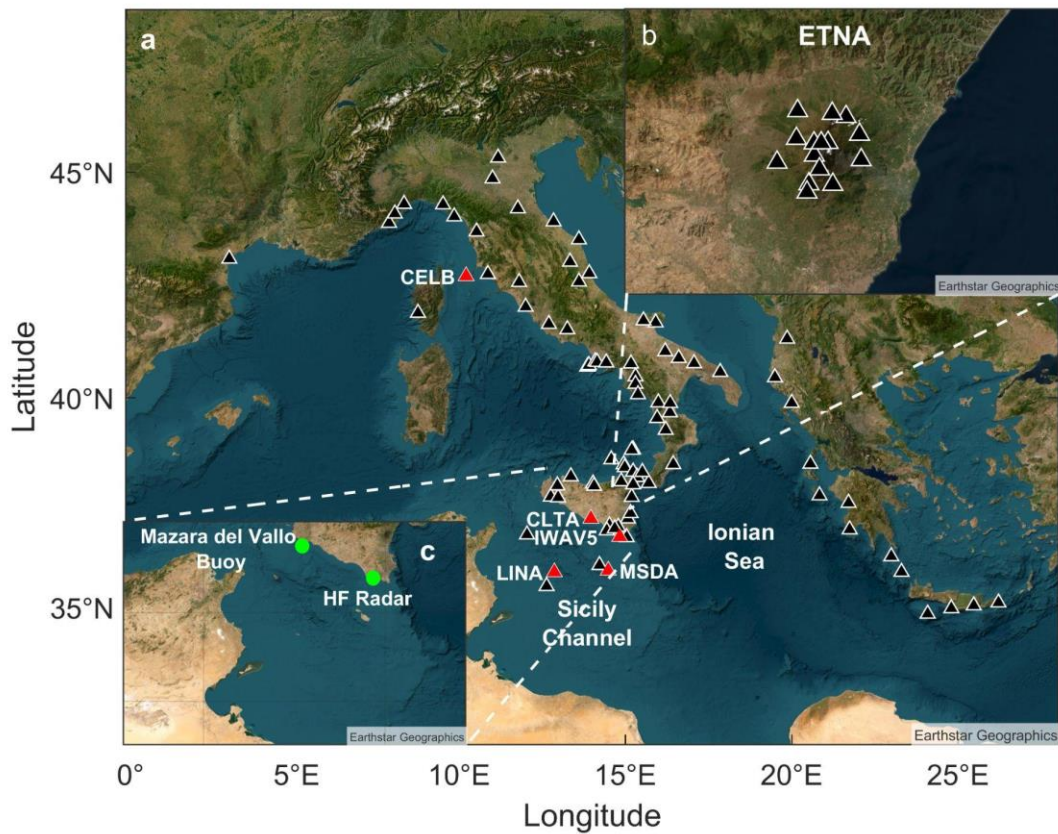
988

989  **Figure 2:** Satellite image of the Mediterranean area with a selection of the broadband seismic

990  stations available in the ORFEUS and INGV databases and used in the spectral analysis and in

991  the grid search method (a) and selection of the broadband seismic stations in the Etna area

992  maintained by INGV-OE (b), used in the array analysis (base image source ©Earthstar

993  Geographic). The red triangles indicate the stations used in the detailed analysis shown in

994  Figures **3** and **9** and in **Supplementary Figures 1** and **2**. The green dots in (c) indicate the

995  position of the wavemeter buoy (Mazara del Vallo) and of the HF Radar (Marina di Ragusa)

996  used for the sea state monitoring.

997
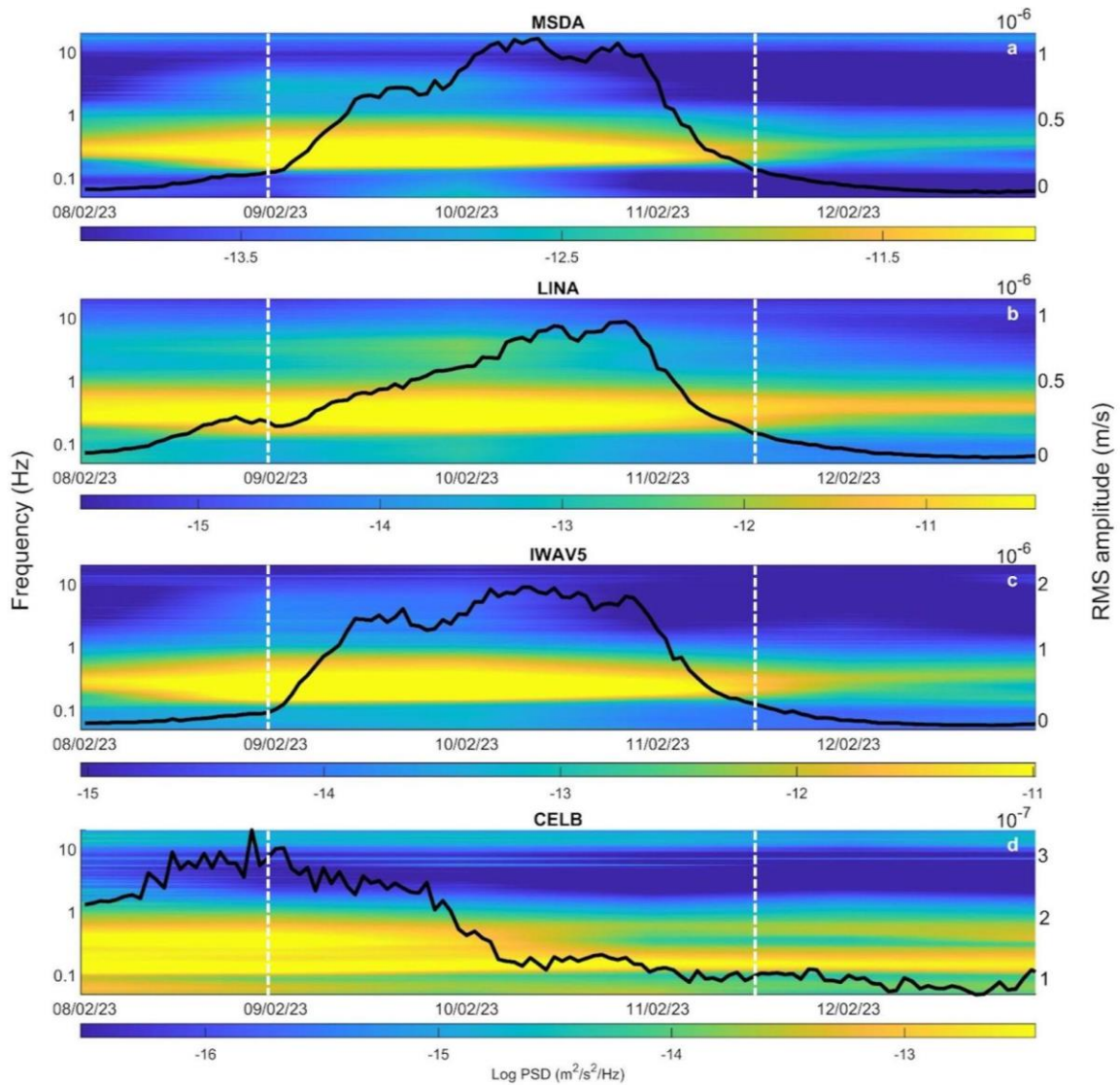
**Figure 3:** Spectrograms and RMS amplitude time series (black lines) for the SM band (0.1-0.2

Hz) of the seismic signal recorded by the vertical component of 4 stations located along the

Maltese coastline (a), in Linosa Island (b), in the southern part of Sicily (c) and in Central Italy

(d) (see **Figure 2a** for the station locations).

1002
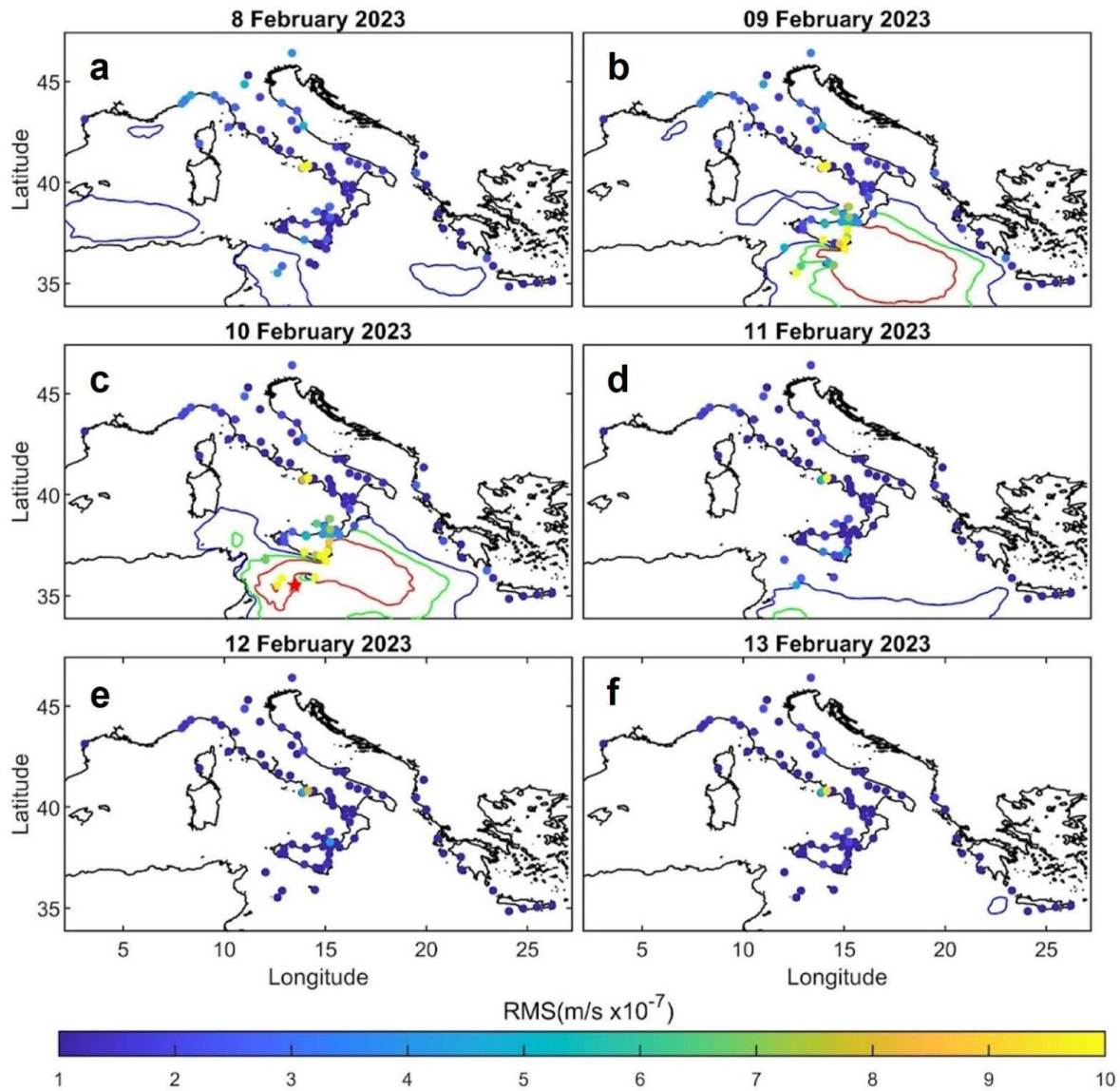
**Figure 4:** Spatial and temporal distribution of the RMS amplitude for the SM band computed at the 105 stations considered (dots). The colors of dots represent the RMS amplitude as specified in the color bar. The blue, green and red contour lines represent significant wave heights of 3, 4 and 5 m, respectively, while the red five-point star in (c) indicates the eye position of the sub-tropical system Helios obtained from satellite images.
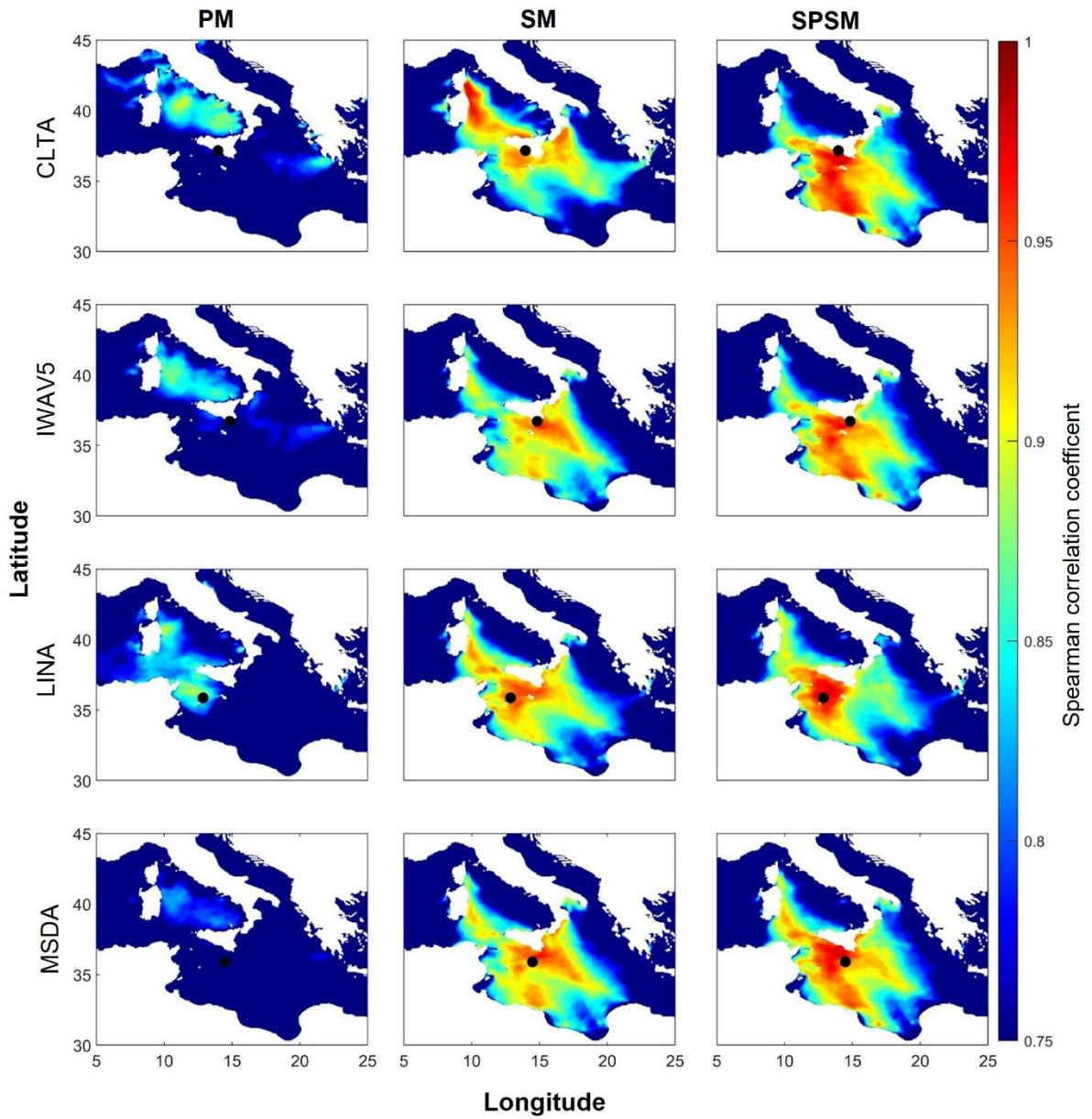
1013

1014    Figure 5:Correlation maps obtained for the vertical component of the seismic stations MSDA,

1015    LINA, CLTA and IWAV5 for the PM, SM and SPSM frequency bands during the period under

1016    investigation. The black dots indicate the position of the seismic station.

1017
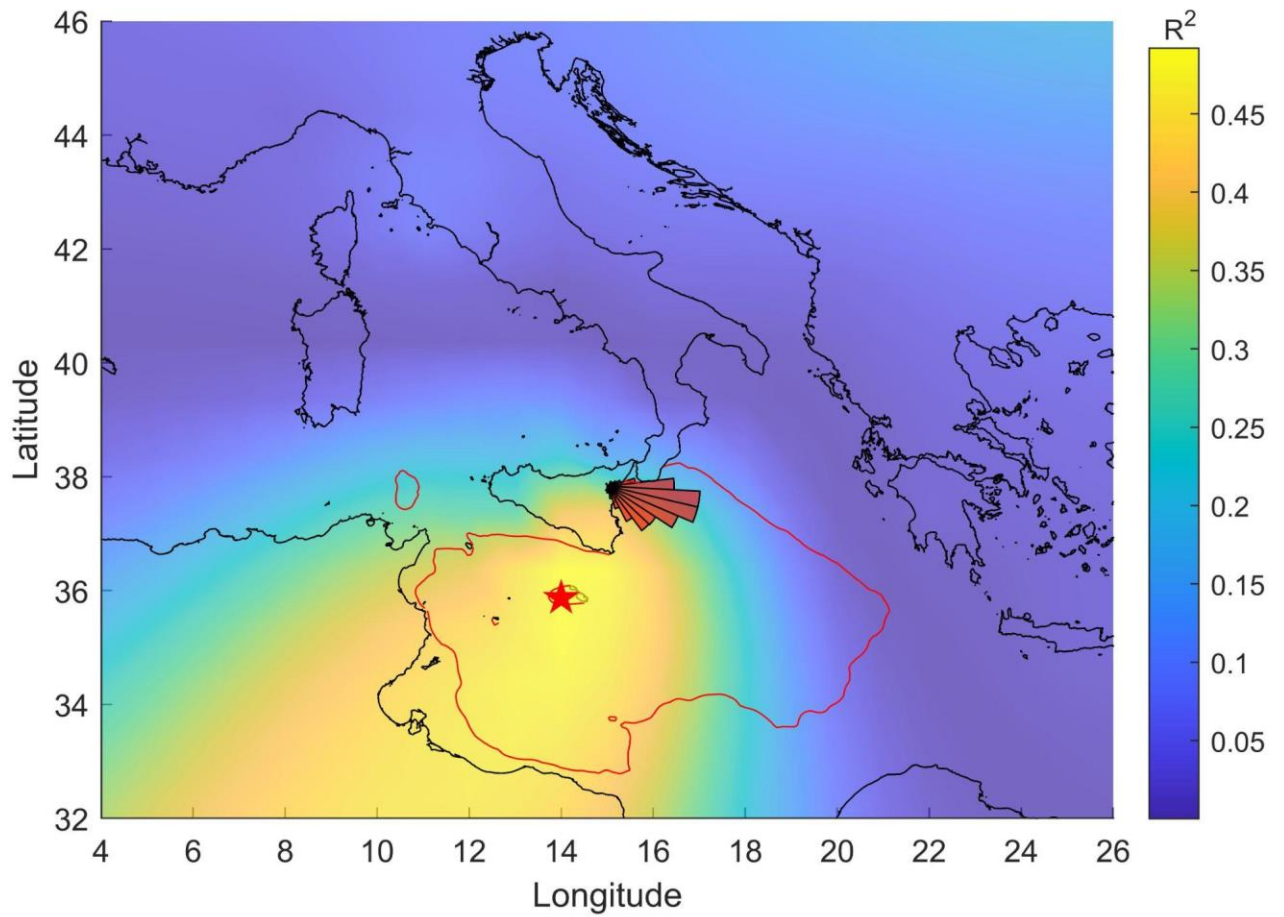
1018

1019 **Figure 6:** Localization of the microseism source for 10 February 2023 at 16:00. The red five-

1020 point star indicates the centroid position of all the grid nodes whose $R^2$ values do not differ by

1021 more than 1% from the maximum $R^2$ value obtained with the grid search method, while the

1022 rose diagram, located at the center of the summit area of Mt. Etna (see **Figure 2b**), shows the

1023 distribution of the back azimuth values on the same day. The red contour line represents

1024 significant wave heights of 4 m obtained from the Copernicus product

1025 MEDSEA_HINDCAST_WAV_006_012 during the same time interval.
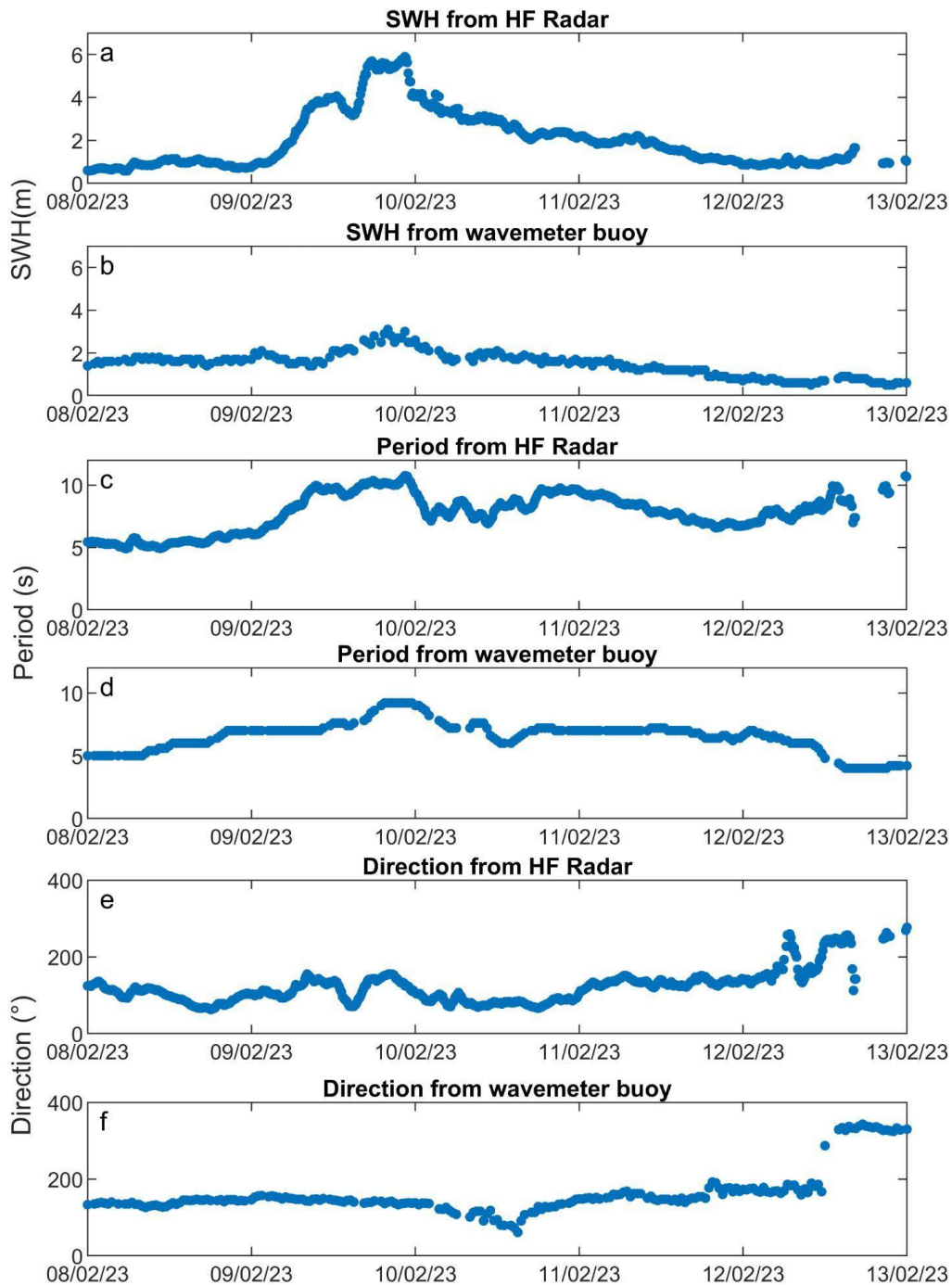
1026
1027 **Figure 7:** Wave features in terms of SWH, period and mean direction time series retrieved by

1028 using the HF Radar (a, c and e) and Mazara del Vallo buoy (b, d and f) data. For the instruments

1029 location see **Figure 2c.**
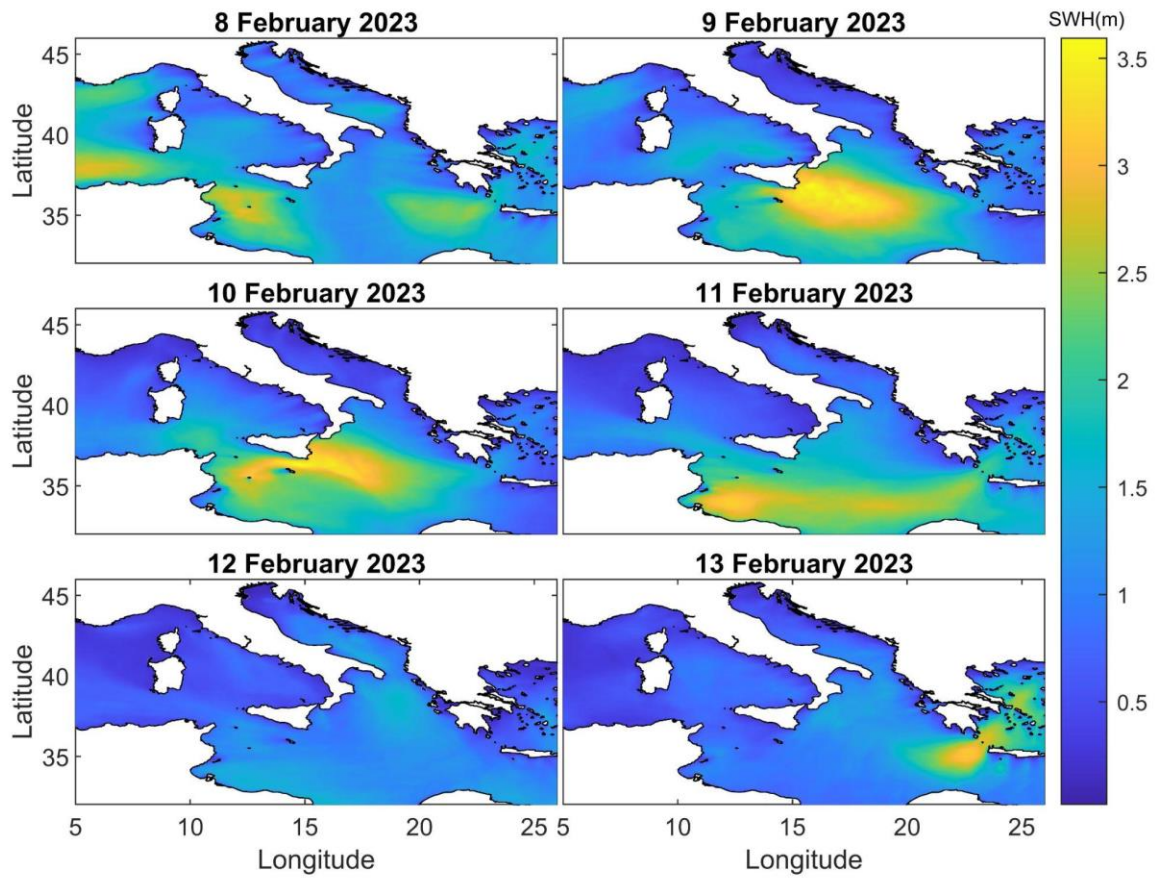
1030
**Figure 8:** Hindcast maps, obtained from the Copernicus product MEDSEA_HINDCAST_WAV_006_012, showing the spatio-temporal variations of SWH during the days taken into account.
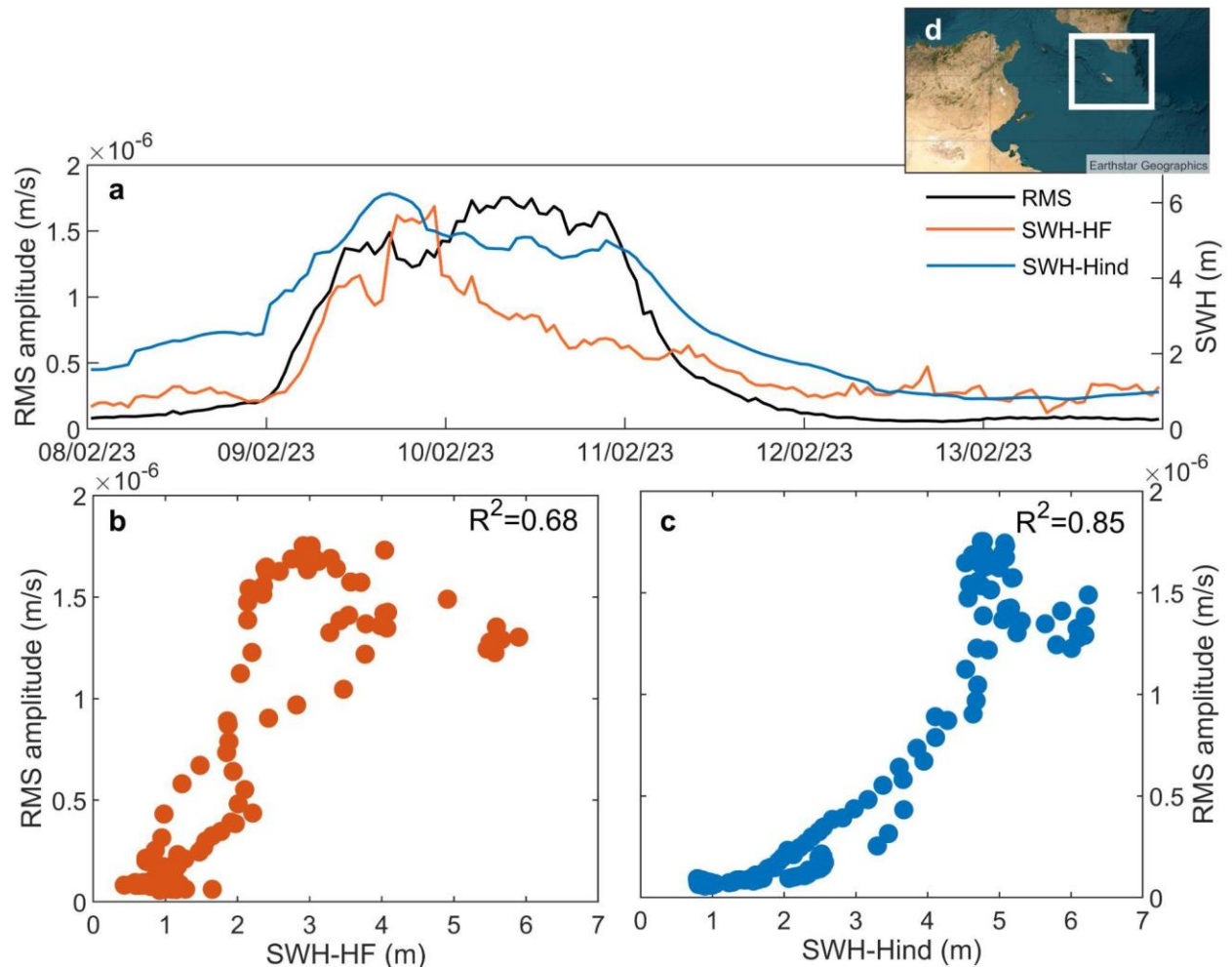
1034

1035 **Figure 9:** (a) RMS amplitude time series, recorded at the station IWAV5, and SWH time series

1036 retrieved by HF Radar (SWH-HF; orange line) and by hindcast data (SWH-Hind; light-blue).

1037 Cross-plot showing the relation between SWH-HF and RMS amplitude (b) and between SWH-

1038 Hind and RMS amplitude (c). The value of the determination coefficient ($R^2$) is reported in the

1039 upper right corner of the plots (b) and (c). In (d) the area of the Sicily Channel used to calculate

1040 the SWH-Hind time series is shown (base image source ©Earthstar Geographic). For the

1041 instruments location see **Figure 2a** and **2c**.
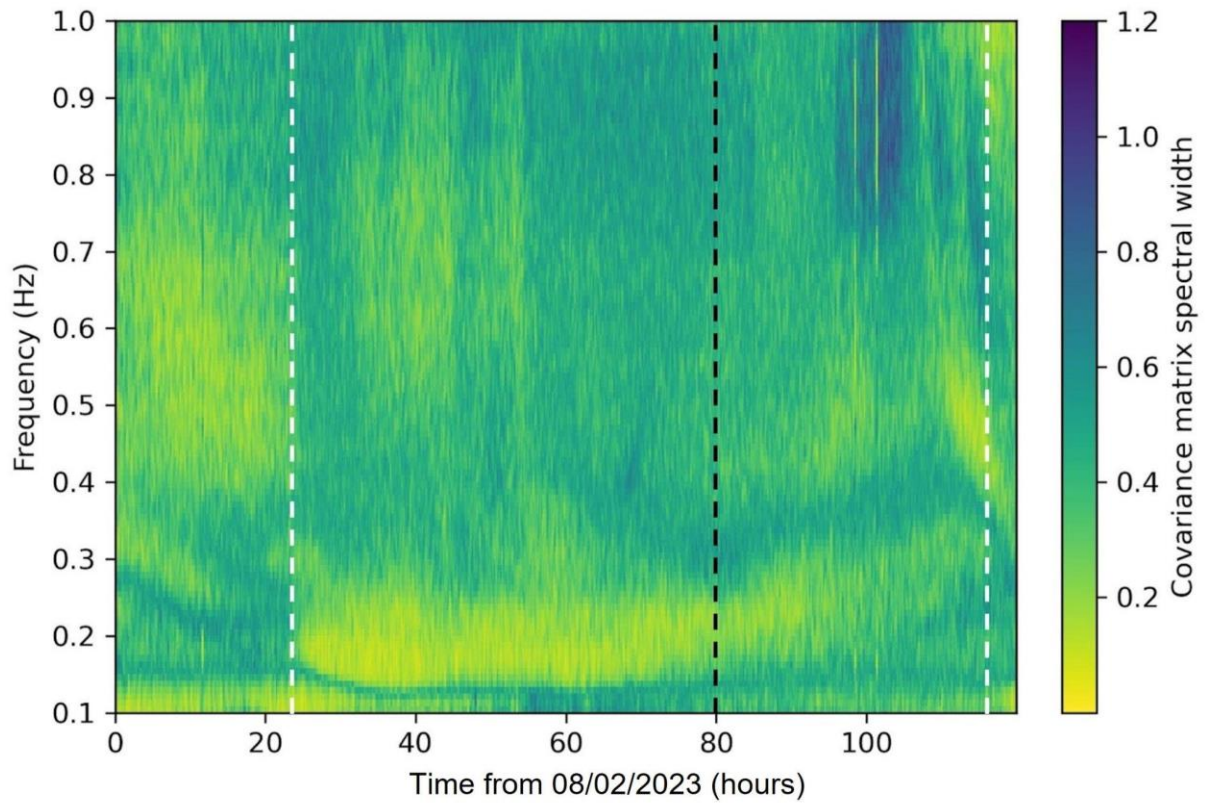
1042

1043    **Figure 10:** Covariance matrix spectral width obtained for the period 8-12 February 2023 using

1044    the stations IWAV5, LINA, MSDA and CLTA. The white dashed lines represent the

1045    development and the ending of the sub-tropical system Helios, while the black dashed line

1046    indicates the time when Helios makes landfall against the Libyan coast. For stations location

1047    see **Figure 2a.**

1048

1049

1050

1051

| Date | Hour | Longitude of microseim source (degrees) | Latitude of microseism source (degrees) | R² Value | Errors latitude (km) | Errors longitude (km) | Longitude of cyclone eye from satellite data (degrees) | Latitude of cyclone eye from satellite data (degrees) |
|---|---|---|---|---|---|---|---|---|
| 09/02/2023 | 08:00 | 15.0000 | 37.3681 | 0.3233 | **243** | **535** | / | / |
| 09/02/2023 | 12:00 | 15.0000 | 36.3681 | 0.3459 | **217** | **412** | / | / |
| 09/02/2023 | 16:00 | 15.0000 | 36.3681 | 0.3554 | **181** | **364** | / | / |
| 09/02/2023 | 20:00 | 15.0000 | 36.3681 | 0.3865 | **173** | **339** | / | / |
| 10/02/2023 | 00:00 | 14.5000 | 36.3681 | 0.4725 | **185** | **298** | / | / |
| 10/02/2023 | 04:00 | 14.5000 | 36.3681 | 0.5066 | **166** | **214** | 14.01584 | 36.24165 |
| 10/02/2023 | 08:00 | 14.3030 | 36.0348 | 0.5107 | **178** | **228** | 13.79612 | 35.57149 |
| 10/02/2023 | 12:00 | 14.3030 | 36.0348 | 0.5091 | **170** | **211** | 13.91697 | 35.13203 |
| 10/02/2023 | 16:00 | 14.0000 | 35.8681 | 0.4920 | **165** | **228** | 13.59836 | 34.5937 |
| 10/02/2023 | 20:00 | 14.0000 | 35.8681 | 0.4762 | **165** | **245** | 13.52146 | 33.59395 |
| 11/02/2023 | 00:00 | 14.0000 | 35.8681 | 0.3864 | **206** | **321** | 13.74118 | 32.9897 |

1053 **Table 1.** Main features of the microseism sources and comparison with the coordinates of the

1054 cyclone eye retrieved from satellite data. The coordinates of the cyclone eye between 8:00 of

1055 9 February and 00:00 of 10 February are absent since the cyclone eye is clearly visible between

1056 01:00 and 23:00 of 10 February 2023.